

Politecnico di Torino

Master's Degree Course
in Nanotechnologies for ICTs

MASTER'S THESIS

PEDOT:PSS: Approaches to enhance the mechanical properties for printed and stretchable electronics

Advisor Home University
prof. Marco Sangermano

Co-Advisor Home University
prof. Fabrizio Pirri

Advisor Host University
prof. Zhenan Bao

Candidate
Andrea Cupertino



Stanford
University

Abstract

PEDOT:PSS is the most successful water-processable conductive polymer. Even though it possesses many unique properties such as the highest reported conductivity among polymers, PEDOT:PSS is characterized by poor mechanical properties in terms of stretchability, stiffness and strength. For this reason, this thesis aims at improving the mechanical properties of PEDOT:PSS. In the first part of the work, the effects of the introduction of ionic additives into the PEDOT:PSS water-dispersion to enhance its stretchability are studied. A process to inkjet printing is then developed to pattern the obtained material and the humidity dependence of the developed printed conductor is evaluated. The printed polymer shows a conductivity ranging from 10 S/cm up to 700 S/cm according to ink composition, stable under 25 % strain and the application as humidity sensor is demonstrated.

The second part of the work deals with the improvement of stiffness and strength by adding nanocellulose as reinforcing agent. A protocol to blend PEDOT:PSS with nanocellulose to obtain a conductive composite is thus reported. The developed composite is further mixed with DMSO, thanks to which it exhibits one of the highest conductivity values ever reported for a PEDOT:PSS/cellulose blend. The conductivity at high cellulose concentration exhibits an exponential decay, which indicates a conduction mechanism based on percolation.

The development of PEDOT:PSS conductors with improved mechanical properties will allow to create stretchable and strong materials capable to bring electronics off the desktop and out into everyday objects

Acknowledgments

This thesis presents the results of six months of research conducted in the Bao Research Group at Stanford University. During this time, I was supported by many people who contributed in different ways and without whom this work would not have been possible. My sincerest gratitude goes to my advisor at the Stanford University, prof. Zhenan Bao, that gave me the opportunity to join her group and that believed in me. I would like to thank my advisor at Politecnico di Torino, Prof. Marco Sangermano, for his high availability and the nice discussions. I am grateful with Dr. Jeffrey B.-H. Tok, for being so helpful and available. Special thanks must be made to Dr. Ulrike Kraft and Dr. Thomas Oehlund, my supervisors for daily activities and experiments. I have felt privileged to be followed by them and experience the kindly, friendly and supportive supervision. I would like to express my gratitude to all the members of Bao Research Group for their help during the thesis and the nice discussions. Last but not least, I would also like to thank all my colleague, not only for the help in all the exams and the projects done during these two year of master, but also for always being there to help and support me as friends.

Contents

Introduction	1
Inkjet printing of intrinsically stretchable PEDOT:PSS	2
Highly conductive PEDOT:PSS/cellulose composite	2
Structure of the thesis	3
1 Theoretical background	5
1.1 Electrically conductive polymers and PEDOT:PSS	5
1.1.1 Conjugated Polymers	6
1.1.2 Conduction mechanism	7
1.1.3 PEDOT:PSS	8
1.1.4 Stretchability enhancers	10
1.2 Elastomeric Substrate	11
1.3 Cellulose	12
1.3.1 Cellulose Nanoparticles	13
1.4 Inkjet Printing	14
1.4.1 Working principle	14
1.4.2 Surface activation	15
2 Materials and Methods	19
2.1 Materials	19
2.2 Substrate preparation	19
2.3 Printing	21
2.4 PEDOT:PSS/cellulose composite preparation	22
2.5 Contact evaporation	23
3 Characterization	25
3.1 Resistance evaluation	25
3.2 Morphological characterization	25
3.3 Humidity measurements	27
3.4 Mechanical Measurements	27
3.5 Adhesion evaluation	28
4 Inkjet printing of intrinsically stretchable PEDOT:PSS	31
4.1 Surface activation	31
4.2 Conductivity	34
4.3 Humidity dependence	35
4.4 Spincoating comparison	38

4.5	Stretchability	40
5	Highly conductive PEDOT:PSS/ cellulose composite	43
5.1	Influence of cellulose nanoparticles on conductivity	43
5.2	Conductivity enhancement	45
5.3	Percolation in the PEDOT:PSS/cellulose composite	48
5.4	Influence of cellulose nanoparticles on transparency	50
6	Conclusion	51
6.1	Inkjet printing of intrinsically stretchable PEDOT:PSS	51
6.2	Highly conductive PEDOT:PSS/cellulose composite	52

Introduction

In 1988 the PARC computer scientist Mark Weiser coined the term “ubiquitous computing” to describe a scenario in which everyday objects are equipped with computational capability to make them communicate and perform tasks without the user’s interaction. [1]. In Weiser’s view, ubiquitous computing represented a human-centric future in which “computer will be so exciting, so wonderful, so interesting, that we never want to be without it” [1]. A similar concept was at the basis of another scenario called “pervasive computing”. The term was introduced by IBM in 1990 to define a distributed computing model composed by dispersed objects interconnected among each other [2]. Nowadays the two terms are considered synonyms. Since then, this paradigm gained ever-growing industrial and academic interest leading to the birth of “Internet-of-Things” (IoT) in 1999 [3]. As the name suggests, it indicates the network of physical devices equipped with computational capability.

The implementation of pervasive computing and IoT requires materials capable to bring electronics from desktop and portable devices to everyday objects, which need to exhibit specific functionalities such as transparency, stretchability, flexibility, lightness, and they need to be cost-effective, a tough combination for silicon technologies. On the contrary polymers possess desirable mechanical and optical properties combined with tunable electrical conductivity. Moreover, they can take advantage from inexpensive printing methods [4]. Thanks to the long history of graphic printing, a wide range of high-quality and cost-efficient printing methods can be adapted to electronics. Among those, inkjet printing is of great interest because its fully digital nature, which make it well suited for low-volume applications. Hence the development of conductive polymers with high performances is a paramount for the implementation of pervasive computing.

Poly(3,4-ethylenedioxythiophene) poly(styrene sulfonate) (PEDOT:PSS) is currently the most successful water-processable conductive polymer with the highest reported conductivity [5]. It is widely used as hole injection material for organic light-emitting-diodes (OLEDs) and polymer photovoltaic cells, as a conductive material for organic field-effect-transistors (OFETs) and touchscreen, as a active material for gas and humidity sensors [6]. Despite that, the low stretchability and the brittleness limit its adoption for many applications within pervasive computing. Therefore, in the frame of this thesis, we aim at improving these two mechanical properties following two approaches. The first approach focuses on the enhancement of stretchability by incorporating ionic additives. Building on the results obtained by Bao et al. [7], we developed an ink for inkjet printing to fabricate stretchable conductors. The humidity dependence of the printed features was then studied. The second approach focuses on improving stiffness and ductility by embedding nanofibrillated cellulose into PEDOT:PSS, in order to obtain a homogeneous high conductive composite.

Inkjet printing of intrinsically stretchable PEDOT:PSS

A stretchable conductor can be obtained via three main routes: embedding it into insulating elastomeric materials, patterning it into sinusoidal structures and incorporating additives to create an intrinsically stretchable material [8]. Despite the versatility and the large number of materials, the first route exhibits a conductivity high strain-sensitivity and percolation dependent, resulting in a poor cycling stability. In the second approach a non-stretchable material is pattern into sinusoidal structures a deposited wich can be elongated when the supporting elastomeric substrate is stretched. This method is mainly limited by the complexity in fabrication and the low device density which can be achieved. An intrinsically stretchable conductor, on the contrary, allows to obtain a conductive material low strain-sensitivity, without, readily solution-processable and compatible with printing methods.

Several studies showed that an intrinsically stretchable PEDOT:PSS can be developed by incorporating surfactants, such as Zonyl or Triton [9, 10], or ionic liquids. Surfactants allow to enhance the stretchability as the expense of conductivity; instead ionic liquids enable to obtain a high conductive film with a stretchabiliy up to 800 % [7]. However the adoption of these materials require the development of patterning methods. Therefore, we developed a process for inkjet printing of intrinsically stretchable PEDOT:PSS with ionic additives. The printed shows an elastic behavior up to 25 % strain with a conductivity ranging from 10 S/cm up to 700 S/cm according to the used ionic additive. We also studied the performance of the developed PEDOT:PSS stretchable conductor for humidity sensing applications.

Highly conductive PEDOT:PSS/cellulose composite

The structural integrity of PEDOT:PSS films is another crucial limitation. its brittleness makes it non-ideal for many applications [11]. Therefore, a supportive substrate have been widely used as reinforcing layer for PEDOT:PSS. However, the perfomances of the resulting conductive materials are highly dependence on the adhesion between substrate and PEDOT:PSS, leading to a vulnerability of the overall system. On the contrary embedding reinforcing agents into PEDOT:PSS results in a homogenous system. One possible candidate as reinforcing agent is cellulose. Thanks to its many hydrogen bondings among glucose units, it shows a Young's Modulus of over 140 GPa with a theoretical Tensile Strength of 0.3 – 22 GPa [12]. Moreover, it presents several additional advantages such as abundance in nature, sustainability, biodegradability, renewability and lightness.

Several attempts have been done to embed cellulose with PEDOT:PSS. Lay et al. embedded Tempo-oxidized nanofibrillated cellulose with PEDOT:PSS by in situ chemical polymerization resulting in a conductivity of only 2.58 S/cm. [13]. A similar conductivity value was obtained by Hafez et al. for a film of PEDOT:PSS with wood microfibers prepared by oxidative polymerization [11]. A notable improvement was achieved by Malti et al., who doped PEDOT:PSS with DMSO prior to mixing it with Tempo-oxidized nanofibrillated cellulose, obtaining a conductivity of 400 S/cm [14]. However, no studies have been conducted on the effect of different cellulose nanoparticles on the composite conductivity. Building on this, we developed a highly conductive PEDOT:PSS/cellulose composite able to retain the conductivity up to a cellulose content as high as 98 weight %. We also investigated the effect of different cellulose nanoparticles and different dopants on the composite conductivity.

Structure of the thesis

The first chapter gives a theoretical overview of electrical and mechanical properties of the adopted materials: conjugated polymers and PEDOT:PSS, elastomeric substrate for inkjet printing and cellulose nanoparticles. The chapter concludes with a description of inkjet printing, its advantages and its working principals. The second chapter describes the process developed to inkjet print the stretchable PEDOT:PSS conductor on SEBS substrate. Moreover the procedure followed to mix PEDOT:PSS with cellulose nanoparticles is detailed. The third chapter shows all the characterization processes employed to evaluate electrical, mechanical and optical properties of the developed conductors. Moreover, it describes the humidity set-up used to characterize the sensing response of the printed conductor. The last two chapters finally present and discuss the results.

1. Theoretical background

This chapter presents a theoretical overview of electrical and mechanical properties of the different materials studied in this thesis. The first section analyzes the electrical conduction mechanism in conjugated polymers, with a focus on PEDOT:PSS, its conductivity and its stretchability. The following section describes the mechanical requirements for a stretchable substrate and materials commonly adopted. The third section introduces cellulose and its constituent nanoparticles (microfibrils, nanofibrils, nanocrystalline). The last part describes ink-jet printing, its advantages, its working principals and the theory behind contact angle and pendant drop measurements.

1.1. Electrically conductive polymers and PEDOT:PSS

Electrically conductive polymers (ECPs) are a class of π -conjugated polymers that possess electrical, magnetic, and optical properties of metals or semiconductors, combined with mechanical properties and processability of organic polymers [5]. Electrical conduction in polymers was observed for the first time in doped Polyacetylene (PA) (see Figure 1.1), by Shirakawa, MacDiarmid, and Heeger [15, 16], discovery honored with the Nobel Prize in Chemistry in 2000. Despite the high conductivity reported ($\sim 10^5$), the low solution-processability and the instability in air due to oxidative degradation prevented its commercialization. Thus a new class of conductive polymers, with improved properties was developed. Among those, polyaniline (PANI), polypyrrole (PPy), polythiophene (PTh) (see Figure 1.1) and their derivatives are the most stable and conductive, [17]. A remarkable breakthrough was the synthesis of poly(3,4-ethylenedioxythiophene) (PEDOT), a PTh derivative [18], highly stable and conductive due to the low HOMO-LUMO bandgap. Unfortunately PEDOT has a low solubility, which limited its application until a mixture with the water-soluble polymer poly(styrene sulfonate) (PSS) was synthesized by Bayer AG [19].

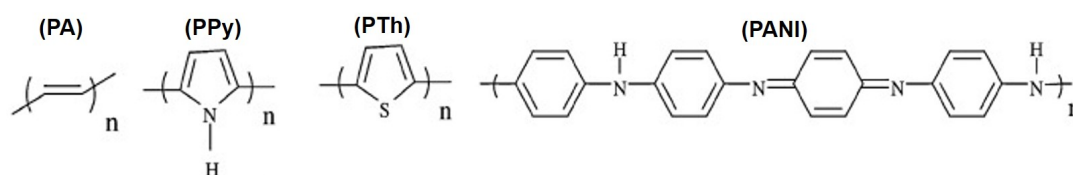


Figure 1.1: Chemical structure of ECPs. From left to right, Polyacetylene (PA), polypyrrole (PPy), polythiophene (PTh), polyaniline (PANI).

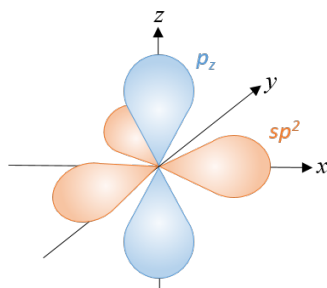


Figure 1.2: orbital structure of an sp^2 hybridized carbon atom.

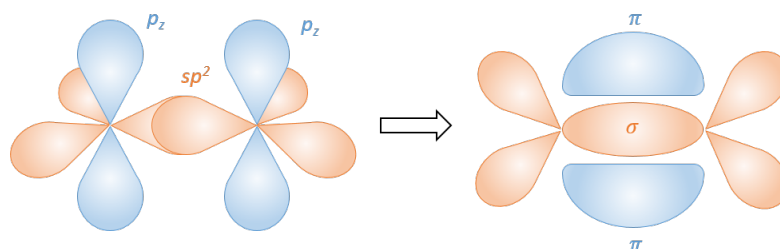


Figure 1.3: Formation of π -bonds and σ -bond starting from two sp^2 hybridized atoms.

1.1.1. Conjugated Polymers

Conjugated polymers are organic macromolecules composed of alternating single and double bonds [20]. This characteristic structure arises from the sp^2 hybridized nature of the carbon atoms involved in the backbone chain. In a hybridized sp^2 atom, $2s$ orbital combines with two of the three available $2p$ orbitals, leading to three sp^2 orbitals, while the other $2p$ orbital remains unchanged. The three sp^2 orbitals thus created are arranged on the same plane along the molecular axis, at an angle of 120° to each other, whereas the $2p$ orbital is arranged perpendicularly to the molecular axis. The resulting orbital structure is depicted in Figure 1.2.

Thanks to such orbital structure, two sp^2 hybridized atoms can create a double bond between them: one σ -bond between two sp^2 orbitals along the molecular axis and one π -bond between two $2p$ orbitals, as shown in Figure 1.3. The electrons contained in the σ -bond are localized between the two atoms due to the high bond strength. On the contrary, the electrons contained in the π -bond are referred to as delocalized due to the low overlapping between the two p-orbitals. Therefore, in a conjugated polymer, the π -bonds do not belong to a specific bond, but are delocalized along the whole chain, as shown in Figure 1.4 for a benzene ring. In consequence it is not possible to describe the chain with only one Lewis structure, but different contributing structures must be used to obtain a description that agrees with the experimental results. These collective structures together constitute a resonance hybrid [21]. A simple example is Polyacetylene (PA), which has two resonant structures characterized by the same energy.

One important consequence of the π -bond overlap is the shortening of the single bond length in a conjugated polymer compared to the normal sigma bond length. This shortening between carbon-carbon atoms brings the electrons density closer to the nuclei of the atoms resulting in an increased stability of the structure [22]. So a conjugated polymer has a higher stability than the same non-conjugated chain. Furthermore, the π -bond overlap and the resulting π -electrons

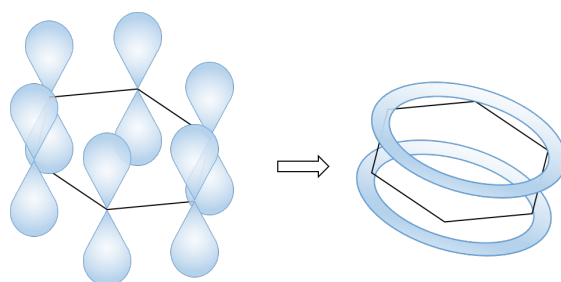


Figure 1.4: Schematic representation of delocalized π -bonds in a benzene ring.

Table 1.1: Line draw and band-gap energy of Polyethylene and Polyacetylene. Alternating of single and double bonds in the latter lowers the energy of the polymer, resulting in a semiconducting behaviour.

Compound name	Band-gap	Line Drawing
Polyethylene	8eV	
Polyacetylene	1.4eV	

delocalization, result in a semiconductive behavior of a conjugated polymer, in contrast with the insulating nature of a non-conjugated one. Going back to the example of Polyacetylene, it has an energy gap of 1.4 eV, for which it can be classified as a semiconductor. Polyethylene, the corresponding polymer with only single bounds between the carbon atoms, has an energy band-gap of 8 eV, under which is categorized as an insulator, as summarized in Table 1.1. Moreover, the bandgap of conjugate polymers becomes smaller with increasing chain length, so for an infinitely long chain a conductive behaviour would be expected. But it reaches a minimum due to Peierls distortion, which arises from the fact that the periodic structure is unstable to dimerization (i.e. two monomers prefer to bond together in a dimer) [23]. In Polyacetylene, the alternation of single and double bonds prevents from forming a metal-like conductor.

On the contrary, aromatic systems (cycling molecules of $4n+2$ electrons, as in benzene), have resonant structures with different energies, as in the case of Polythiophene. The more stable structure is called aromatic, whereas the less stable is called quinoid. In that case the band-gap does not derive from the Peierls distortion, but from the difference in energy [24]. The polymer exhibits two energy values at the same crystal momentum, resulting in a band-gap. Table 1.2 summarizes the band-gap origin in the two cases analyzed.



1.1.2. Conduction mechanism

The electrical conductivity of a material is given by:

$$\sigma = ne\mu \quad (1.1)$$

where e is the electron charge, n is the charge-carrier density and μ is the charge-carrier mobility. A good conductivity requires a high charge-carrier mobility, which in conjugated polymers derives from π -electrons delocalisation along the backbone chain and π -stacking, which aids hopping of charges between neighbouring chains (intra-chain transport) [25]. Furthermore, free charge

Table 1.2: Band gap origin for Polyacetylene and Polythiophene.

Compound name	Band-gap origin	Line Drawing
Polyacetylene	Peierls instability	
Polythiophene	Aromatic and Quinoid structures	

carriers must be generated in the delocalized π -bonds, otherwise the material behaves like an insulator due to the band gap between the highest occupied molecular orbital (HOMO) and the lowest unoccupied molecular orbital (LUMO). The free-charges generation process can be controlled through oxidation and reduction with a molecule called dopant in analogy with the doping in inorganic semiconductors.

It is nevertheless important to underline that the latter is a process substantially different from the one in organic semiconductors. In conventional electronics it defines a substitutional process in which a dopant (donor or acceptor) replaces one atom of the semiconductor in the lattice, without affecting the band structure. By doing that, it normally participates to the electronic structure of the semiconductor in term of filling the gap in the lattice, with a different number of electrons. In organic materials, instead, the process occurs by charge transfer where the dopant is a chemical impurity which transfers its charge to the organic semiconductor affecting the overall band structure [26]. In case of p-type doping, an oxidizing agent added to the organic semiconductor removes one electron from the backbone chain, creating a hole which can propagate through the polymer. Contrary, in case of n-type doping a reducing agent is responsible for adding one electron which can propagate along the chain. The dopant remains as counterion to balance the charge on the conjugated polymer, resulting in a volume expansion and a reduced interaction between delocalized π -electrons. Therefore, doping improves the electrical conductivity but tends to decrease the mechanical properties [27].

1.1.3. PEDOT:PSS

Poly(3,4-ethylenedioxythiophene) (PEDOT) is a conjugated polymer with excellent ability to switch between the insulating state and the conducting state, chemical and environmental stability, low toxicity and good bio-compatibility. Furthermore, it has a low HOMO-LUMO band gap (around 1.6 eV), which can be further decreased below 1 eV if doped, resulting in a highly stable and conductive ECP[6]. It is generated by oxidative polymerization of the monomer EDOT. To overcome its poor solubility, the oxidation is performed in the presence of poly(styrene sulfonate) (PSS), resulting in the aqueous dispersion PEDOT:PSS. In Figure 1.5 it is possible to notice that the PSS not only allows the dispersion of the polymer in water, but acts as dopant.

Experimental evidences proved that the molecular weight of the PEDOT is much lower than the one of PSS [29]. Therefore, it is generally accepted to consider several PEDOT oligomers bond to a single PSS polymer chain. To shield the hydrophobic PEDOT from the water, the polymer arranges in a grain structure with a PSS-rich shell and a PEDOT-rich core. A model proposed by Lang et al. describes each grain composed by several PSS with a coil conformation. The chains in the center have an even distribution of PEDOT oligomers, while on the edge, a non-uniform arrangement of PEDOT leads to the PSS-rich shell[29]. The model is depicted in Figure 1.6. It is furthermore assumed that the grains are tight together by hydrogen bonds

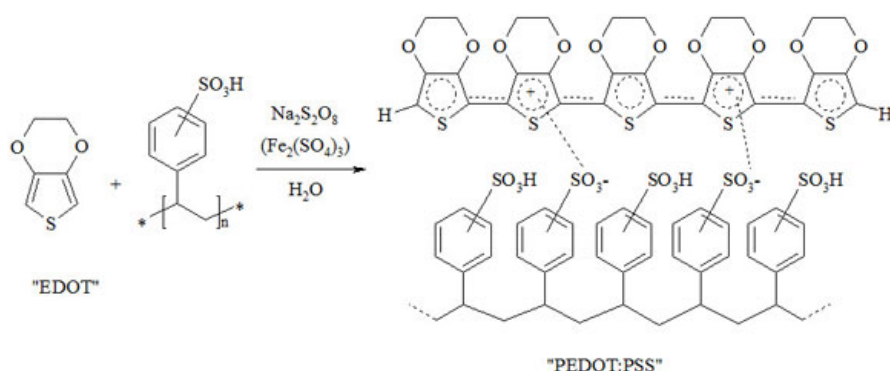


Figure 1.5: Chemical structure of PEDOT:PSS. The positive charges of PEDOT are bound with the negative charges of PSS by Coulomb interaction. Adapted from [28]

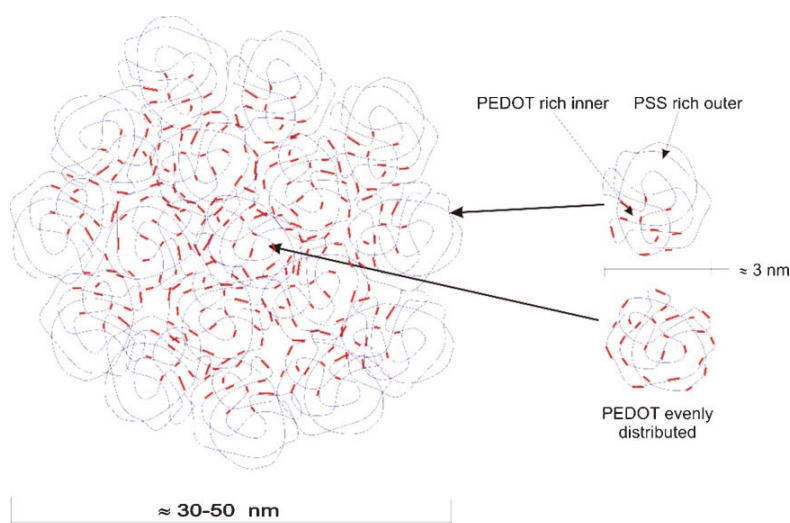


Figure 1.6: Schematic representation an individual PEDOT:PSS grain. Adapted from [29]

among the HSO_3 groups of PSS [30], as shown in the Figure 1.7.

Stöcker et al. showed that the electrical conductivity in PEDOT:PSS can be considered as a percolation between sites of height conducting PEDOT:PSS complexes in a matrix of excess height resistive PSS [31]. Therefore increasing the content of PSS does not affect the doping level and the charge-carrier density, which remains constant, but it results in a lower conductivity due to the decrease of charge-carrier mobility [31]. Different conductivity values ranging from 0.2 mS/cm to 1 S/cm can thus be obtained according to the PEDOT:PSS ratio. All the experiments were performed with the height conductive formulation (Clevios PH1000) with a PEDOT:PSS ratio of 1:2.5 and specific conductivity value lower than 1 S/cm.

This value can be enhanced to more than 800 S/cm by adding dimethyl sulfoxide (DMSO), as shown for the first time by Kim et al. in 2002 [32]. Since then, many methods have been investigated to improve the poor conductivity of pristine PEDOT:PSS. These comprise physical methods as light and heat treatments, as well as chemical methods as additive treatments and post-treatments [33]. A very important class of chemical additives is high boiling point

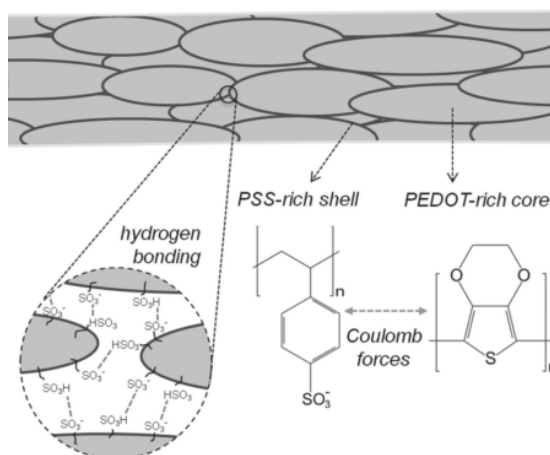


Figure 1.7: Morphology of PEDOT:PSS film consisting of grains with PEDOT-rich core and PSS-rich shell bounds by Coulomb force. It is assumed that the grains are tight together by hydrogen bonds among the HSO_3 groups of PSS. Adapted from [30].

solvents and other polar compounds usually called "secondary dopants" because the conductive enhancement effect is independent whether the additives remain in the dried film or not [6]. The concept of secondary doping, introduced in 1993 for Polyaniline, defines a process in which the enhanced properties persist even upon complete removal of the additive [34]. The enhancement mechanism is not completely understood, however most of the works in literature agree that it is based on a change of the PEDOT:PSS morphology [35]. The rearrangement results in a lower resistance between the dried grains and in an overall higher conductivity up to more than two orders on magnitude. Additional post-treatment processes with acids allow to further increase the conductivity up to 3 orders of magnitude compared to the pristine PEDOT:PSS value. The acid post-treatment results in an improved crystalline structure of the PEDOT, facilitating the inter-chain as well as intra-chain transport [36]. Another relevant conductivity enhancement process is based on the phase separation between PEDOT and PSS, removing the excess PSS in the film with alcohol as Methanol [37].

1.1.4. Stretchability enhancers

Pristine PEDOT:PSS is characterized by a poor stretchability with a fracture strain as low as 5% [9] and a Young's modulus of 2 GPa [38]. The stretchability can be enhanced by increasing the disorder among the polymeric chains, though resulting in a lower conductivity due to the decreased crystallinity. Recent studies showed that addition of a nonionic fluorosurfactant polymer (Zonyl) combined with DMSO leads to an increased fracture strain as high as 188% strain [9]. However, the material exhibits an elastic behaviour only up to 10% strain with a reversability up to 30% strain, with a lower conductivity, highly degraded at maximum strain. Another plasticizer reported as PEDOT:PSS conductivity and stretchability enhancer is Triton X-100, [10, 37], a nonvolatile surfactant able to lower the Young's Modulus and increases the fracture strain up to 60%. The addition of surfactant results in the formation of PEDOT nanofibril, leading to an additional increase of conductivity. Despite that, the latter is highly strain sensitive with a maximum value lower than 100 S/cm.

Bao et al. reported in 2017 a new approach able to overcome the trade-off between stretch-

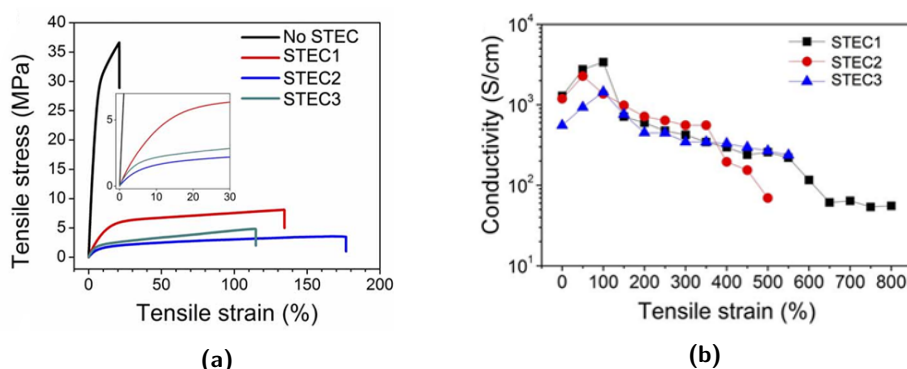


Figure 1.8: (a) Stress/strain curve of pristine PEDOT:PSS (no STEC) and with three different STEC enhancers, (b) conduction under different strain of PEDOT:PSS with STEC enhancers. Adapted from [7]

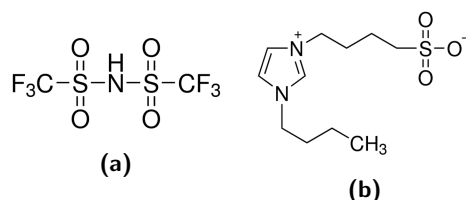


Figure 1.9: (a) Bis(trifluoromethane)sulfonimide chemical structure, (b) 4-(3-Butyl-1-imidazolio)-1-butanefulfonate chemical structure.

ability and conductivity by incorporating "ionic additives-assisted stretchability and electrical conductivity (STEC) enhancers" to PEDOT:PSS [7]. As shown in Figure 1.8a, the obtained material exhibits a low Young modulus with an high fracture strain, caused by a morphology rearrangement. The study shows that ionic additives also act as dopants due to the highly acidic anions, leading to a conductivity higher than 3000 S/cm which does not degrade with strain (see Figure 1.8b). The work described the effects of several ionic additives, all showing high stretchability combined with different conductivity values ranging from less than 1 S/cm to more than 3000 S/cm. In the experiments performed in this thesis we decided to work with Bis(trifluoromethane)sulfonimide lithium salt (STEC 1) (see Figure 1.9a) and 4-(3-Butyl-1-imidazolio)-1-butanefulfonate (STEC 2) (see Figure 1.9b). The former leads to high conductivity combined with a Young's Modulus of 55 MPa, while the latter results in a low conductivity equal to 3.4 S/cm and a Young's Modulus as low as 34 MPa.

1.2. Elastomeric Substrate

The performance of a stretchable system is highly influenced by the chosen substrate material. Not only must it provides good support and good adhesion to the active components, but it must also fulfill different elastic requirements. Consequently, different aspects must be taken into consideration to select a substrate material. Firstly, the material should be highly stable and chemically inert with respect to the solvents used for the fabrication of the active components, in order to prevent damages during the process. Secondly, it must exhibit high surface

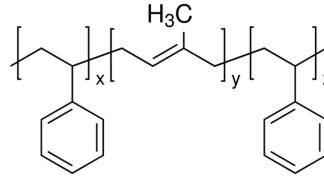


Figure 1.10: Chemical structure of Poly[styrene-*b*-(ethylene-co-butylene)-*b*-styrene] (SEBS).

energy to improve the bond with the active components [39]. In a stretchable system the elastic performance is highly affected by the adhesion of the active components with the substrate. In addition, it must exhibit height and reversible stretchability with good cycling stability.

For these reasons, entropy-elastic elastomer, which be easily stretched while their volume remains constants, are the materials commonly adopted. Among them, Polydimethylsiloxane (PDMS) is the most widely used due to the simple preparation process, the commercial availability and the good stability. However, it has a restricted stretchability range, less than 200%, which prohibits its application to highly stretchable devices. A valid alternative is Poly[styrene-*b*-(ethylene-co-butylene)-*b*-styrene] (SEBS), a transparent hydrogenated styrenic thermoplastic elastomer with an elongation up to 700% [40]. Figure 1.10 shows the chemical structure of SEBS [8].

1.3. Cellulose

Cellulose is the most abundant biological polymer on earth[41]. It is produced by different source materials: (a)wood, (b)plant, (c)tunicate, (d)algae, (e)bacteria. The focus of this section is on wood cellulose, which offers two import advantages, the abundance and the existing infrastructure for harvesting and processing it[42].

Wood has a hierarchical and mesoporous structure composed of around 40 wt% by well oriented cellulose microfibrils, each constitute by thousands of semicrystalline nanoparticles (nanofibers and nanocrystals)[43]. The latter are crosslinked by hemicellulose (25 wt%), a polysaccharide made of short chains of sugar monomers. The remaining 35 wt% is composed of lignin which aids to form a strong and stiff material.

Cellulose is a linear chain of thousands of $\beta(1 \rightarrow 4)$ linked D-glucose units [44]. Each unit is composed by two glucose rings linked together by a covalent bond between the carbon atom C1 of one glucose ring and the carbon atom C4 of the next glucose ring, as depicted in Figure 1.11. The polymer has the formula $(C_6H_{10}O_5)_n$.

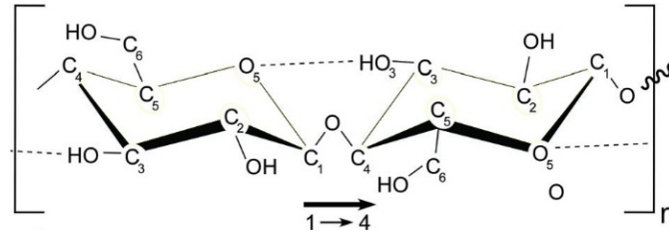


Figure 1.11: Schematic of the single unit of the cellulose chain composed by $\beta(1 \rightarrow 4)$ linked D-glucose units.

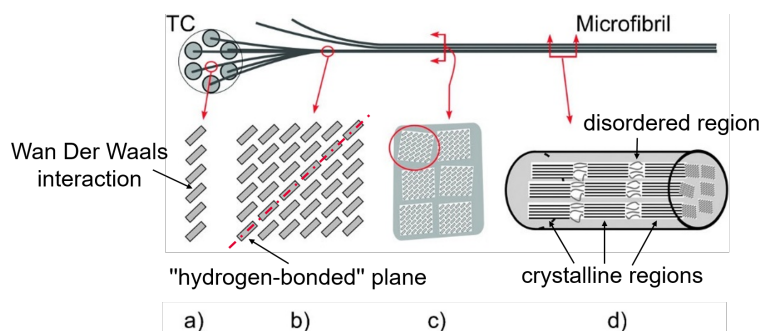


Figure 1.12: Hierarchical structure of a cellulose microfibril. (a) subunit cross-section, (b) nanofibril cross section, (c) microfibril cross-section, (d) microfibril transverse view. Adapted from [42]

The linkage between glucose units in the chain is stabilized by intra-chain hydrogen bonds between the hydroxyl group of one glucose ring and the oxygen atom of the adjacent one, shown by dotted lines in Figure 1.11, resulting in a linear configuration [42]. Different chains are tight together with Wan Der Waals interactions and inter-chain hydrogen bonds between the hydroxyl group of one glucose ring and the oxygen atom of adjacent molecule. It has been observed that the intra and inter-chain hydrogen bonds in Cellulose I, the cellulose structure derived from wood, are most prevalent along one crystalline plane, for that reason called "hydrogen-bonded" plane [45, 46, 47]. Along the other planes, Van Der Waals forces dominate the attraction between cellulose chains over intra-chain hydrogen bonds, leading to a low degree of crystallinity [48, 46].

Figure 1.12 shows a schematic of the hierarchical structure of a cellulose microfibril. The single subunit is composed by cellulose chains bond together by Van Der Waals forces as shown in Figure 1.12a. Different subunits, linked by hydrogen bonds, form an elementary fibril, depicted in Figure 1.12b. Several fibrils can further aggregate in a microfibril, shown in Figure 1.12c. The single subunits are composed by alternating crystalline regions and amorphous regions. It follows that also elementary fibrils and microfibrils exhibit the same structure as depicted in the transverse section in Figure 1.12d.

1.3.1. Cellulose Nanoparticles

Cellulose can be isolated from lignin and hemicellulose with purification and homogenization pretreatments [42]. Then mechanical, chemical and enzymatic processes allow to separate it into the constitutive nanoparticles [49]. Depending on the process used, nanoparticles with different sizes and structure can be extracted. The four particles types considered in this thesis are (a) Nanocrystalline cellulose (NCC), (b) Nanofibrillar cellulose (NFC), (c) TEMPO-oxidized Nanofibrillar cellulose (Tempo NFC) and (d) Microfibrillar cellulose (MFC).

Microfibrillar cellulose

Microfibrillar cellulose (MFC) is a particle produced by homogenization process of cellulose fiber. According to Meier, MFC does not have defined diameter dimensions [50] because defines a well-defined biological structure found in plant. Despite that, it is commonly accepted to consider $1\mu\text{m}$ as the average diameter of these particles [51]. Its cross-section is shown in Figure 1.12c.

Nanofibrillar cellulose

Nanofibrillar cellulose (NFC) is produced by refining processes of MFC, characterized by a high aspect ratio and containing both amorphous and crystalline regions. NFC can be composed by single (see Figure 1.12b) or multiple elementary fibrils according to the degree of aggregation among the hydroxyl groups of the glucose.

Tempo-oxidized Nanofibrillar cellulose

TEMPO (2,2,6,6-tetramethylpiperidine-1-oxyl radical)-mediated oxidation is a surface modification treatment applied to NFC which oxidizes the hydroxyl group of glucose to the carboxyl group, preventing the elementary fibrils to aggregate. Therefore the resulting Tempo-oxidized Nanofibrils cellulose (Tempo NFC) are mostly composed by elementary fibrils, each consisting of tens of cellulose chains, with high aspect ratio and containing both amorphous and crystalline regions. The cross-section of an elementary fibril can be observed in Figure 1.12b.

Nanocrystalline cellulose

Nanocrystalline cellulose (NCC) is produced by acid hydrolysis of a MFC, by which the amorphous fraction is dissolved. The resulting particle exhibits high aspect ratio and a degree of polymerization between 100 and 200. The transverse view in Figure 1.12d shows the crystalline region which compose NCC.

1.4. Inkjet Printing

Inkjet printing is an additive, fully digital technique, able to create defined patterns without additional patterning steps [52]. It allows to obtain a defined pattern by performing only a single procedure, whereas conventional fabrication techniques would require several processes carried out with different equipments. For instance, a conventional fabrication process involves firstly a deposition step (coating, epitaxy, physical or chemical deposition), followed by lithography and etching steps, leading to a large waste of material and an overall high complexity. On the contrary, a printing technique directly deposit the material in the specific area defined by the pattern, without wasting material. Moreover, thanks to the non contact feature, different kind of substrates can be employed, without in principle any limitation on size, shape or stiffness. These aspects make inkjet printing a powerful technique for patterning devices on low-cost and non-conventional substrates. On the contrary, conventional techniques are still preferable for high-performance applications with minimum features sizes below one micron [53].

Two important aspects that must be considered while dealing with this technique are the adhesion of the ink to the substrate and the proper jetting of the droplets from the printer cartridge. A precipitation of solid in the ink can indeed lead to aggregation and clogging of the nozzles, highly affecting the printing quality. Moreover, the surface tension of the ink and its viscosity must be optimized to reduce ink movement onto the substrate. Various treatments, both to the surface and to the ink, can be applied to overcome these limitations, as discussed in the following section 1.4.2.

1.4.1. Working principle

Inkjet printing is based on individual droplets of ink ejected in a controlled way so as to create a pattern on the substrate. According to the jetting mechanism, two main modes of operation are available: continuous inkjet (CIJ) and drop on demand (DOD) inkjet [55].

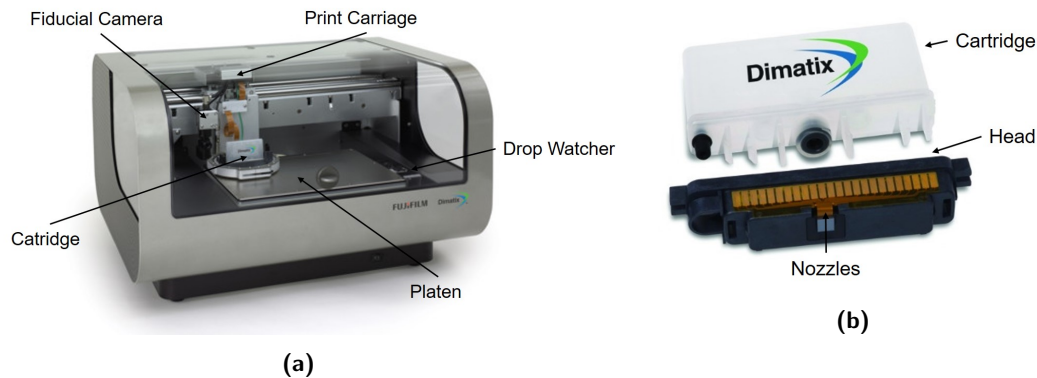


Figure 1.13: (a) Inkjet printer Fujifilm Dimatix DMP-2800 and (b) Cartridge Fujifilm Dimatix DMC-11610, showing the main parts. Adapted from [54]

A continuous inkjet (CIJ) printer continuously ejects droplets from the nozzle through a pressure applied to the ink chamber. Some droplets are then charged before to be ejected. This allows to deflect those droplets towards the substrate with an electrostatic field applied at the output of the nozzles. The non charged droplets are instead collected in a ink catcher and re-used. On the contrary, a drop on demand (DOD) inkjet printer ejects droplets only when an electrical pulse is applied to a transducer connected to the ink chamber. Due to the different mechanism, CIJ printers show higher working frequency, while DOD inkjet printers present a simpler head [55].

The transducer of DOD inkjet printers can be based on a piezoelectric mechanism or on a thermal mechanism. In the first case, the applied electrical pulse is a voltage signal which creates a pressure due to piezoelectric effect. The acoustic wave thus generated is responsible for ejecting one droplet of ink. In the second case, a current pulse is applied to a heating element which causes the evaporation of a small portion of ink. The bubble resulting increases the pressure inside the ink chamber, which propels one droplets out of the nozzle.

All the experiments in this master's thesis were performed with a DOD inkjet printer actuated with a piezoelectric mechanism, the Fujifilm Dimatix DMP-2800 depicted in Figure 1.13a. On the left of the Figure it is possible to see the Print Carriage, which contains the cartridge and a Fiducial camera focused on the substrate. The cartridge is mounted on a rotating holder, which allows to set a tilting angle between the nozzles and the direction of printing affecting the droplet distance. The substrate is loaded on the platen, where it can be fixed under vacuum and heated. An additional camera, the drop watcher, is used to visualize the jetting of the droplets from all the nozzles.

The most important and fragile parts of the equipment are the nozzles, positioned on top of the head of the cartridge, in Figure 1.13b. The nozzles are indeed tens of microns in diameter ($21\mu\text{m}$ for the cartridge used in this work) and can be easily clogged by solid precipitated in the ink. In order to prevent that, the solid particles dispersed in the ink solution should be $1/100^{th}$ the size of the nozzles ($0.21\mu\text{m}$ for this work).

1.4.2. Surface activation

Printing quality is highly dependant on the adhesion between ink and substrate, mainly because of the ink's viscosity and the difference between the substrate surface's energy and the ink's

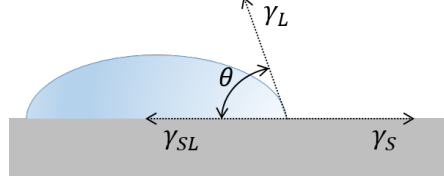


Figure 1.14: Schematic of a liquid droplet on top of a substrate highlighting the quantities of Young equation.

surface tension. If the substrate's free surface energy is indeed lower than the surface tension, the substrate tends to adsorb the ink in order to lower its energy. On the contrary, a low free surface energy can prevent the droplets spreading over the substrate, leading to a non uniform and discontinuous pattern.

By considering a sessile droplet, the two quantities are related by means of the Young's equation:

$$\gamma_S = \gamma_{SL} + \gamma_L \cos \theta \quad (1.2)$$

where γ_S is the free energy of solid/air interface per unit surface area (i.e. solid surface energy), γ_{SL} is the free energy associated with the liquid/liquid interface per unit area (i.e. solid/liquid interface energy), γ_L is the free energy associated with the liquid/air interface per unit area (i.e. surface tension), θ is the contact angle between the liquid and the solid. Figure 1.14 shows all the forces acting on a liquid sessile droplet.

Substrate's surface free energy

In order to extract the surface's free energy from the Young's equation 1.2, the solid/liquid interfacial energy γ_{SL} must be known. In the Fowkes method the latter is expressed as a function of the two surface energy γ_L , γ_D and the interaction between their polar and dispersive components:

$$\gamma_{SL} = \gamma_S + \gamma_L - 2(\sqrt{\gamma_S^d \gamma_L^d} + \sqrt{\gamma_S^p \gamma_L^p}) \quad (1.3)$$

where:

$$\gamma_L = \gamma_L^d + \gamma_L^p \quad \text{and} \quad \gamma_S = \gamma_S^d + \gamma_S^p \quad (1.4)$$

Building on this method, Owens and Wendt, substituted the 1.3 into the Young's equation 1.2, so as to obtain an expression of the substrate's surface energy depending only on the contact angle and the surface tension [56]:

$$\frac{1 + \cos(\theta)}{2} \frac{\gamma_L}{\sqrt{\gamma_L^d}} = \sqrt{\gamma_S^p} \sqrt{\frac{\gamma_L^p}{\gamma_L^d}} + \sqrt{\gamma_S^d} \quad (1.5)$$

By knowing the contact angles and the surface tension of at least two liquids, the equation 1.5 allows to determine the value of the free surface energy γ_S by linear regression.

Ink's surface tension

One of the most used methods to extract the surface tension of a liquid is the pendant drop technique, based on an iterative comparison of the profile of a pendant drop with the theoretical

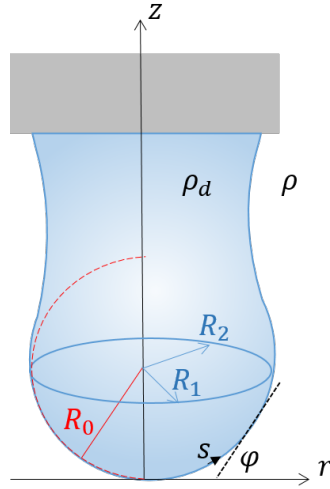


Figure 1.15: Schematic of a pendant drop highlighting the quantities in Young-Laplace equation.

value expected from the Young-Laplace equation [57]. The latter allows to describe a pendant drop at mechanical and hydrodynamic equilibrium:

$$\gamma_L \left(\frac{1}{R_1} + \frac{1}{R_2} \right) = \Delta P \quad (1.6)$$

where γ_L is the surface tension, ΔP is the Laplace pressure at the interface, R_1 and R_2 are the principal radii of curvature (see Figure 1.15). The Laplace pressure can also be expressed in term of the pressure ΔP_0 at the apex of the drop ($z = 0$) and the hydrostatic pressure:

$$\Delta P = \Delta P_0 - \Delta \rho g z \quad (1.7)$$

where g is the gravitational force and $\Delta \rho$ is the difference between the density of the two fluids ρ_d and ρ (see Figure 1.15).

By transforming Equation 1.6 into cylindrical coordinates r , z and ρ , a set of differential equations as a function of the arc length s from the drop apex is obtained:

$$\frac{d\varphi}{dS} = 2 - BZh - \frac{\sin(\varphi)}{R} \quad (1.8a)$$

$$\frac{dR}{dS} = \cos(\varphi) \quad (1.8b)$$

$$\frac{dZ}{dS} = \sin(\varphi) \quad (1.8c)$$

where Z , S and R are the dimensionless forms of the variables z , s and r , scaled by the radius of curvature R_0 at the drop apex. B denotes the Bond number[58], a dimensionless quantity which link the surface tension to the drop profile:

$$B = \frac{\Delta \rho g R_0^2}{\gamma_L} \quad (1.9)$$

This set of differential equation with the boundary conditions:

$$Z = S = R = \varphi = 0 \quad (1.10)$$

allows then to know the value of the associated Bond number 1.9, by which the surface tension is extracted.

2. Materials and Methods

This chapter contains materials and methods used in this thesis. The first section explains the protocol followed to print the stretchable PEDOT:PSS ink onto the SEBS substrate, with a detailed description of the inkjet printing process. The second section presents the preparation of nanocellulose/PEDOT:PSS composite. The last section describes the metal electrodes evaporation procedure.

2.1. Materials

All processing solvents, such as toluene, 2-propanol, and acetone were purchased from commercial sources and used as received. Poly(3,4-ethylenedioxythiophene)-poly(styrenesulfonate) (PEDOT:PSS) PH1000 aqueous dispersion (1.3 wt %) were obtained from Clevios. Dimethyl sulfoxide (DMSO), ethylene glycol, polyethylene glycol (PEG), chloroform, hexadecane, diiodomethane, Bis(trifluoromethane) sulfonimide lithium salt (STEC 1) and 4-(3-butyl-1-imidazolium)-1-butanedisulfonate (STEC 2) were obtained from Sigma-Aldrich.

The commercially available Polystyrene-block-poly(ethylene-ran-butylene)-block-polystyrene (SEBS) Tuftec H1062 was supplied from AK Elastomer.

Nanofibrillated cellulose (NFC) aqueous suspension (3 wt%), Tempo-oxidized Nanofibrillated cellulose (Tempo NFC) aqueous suspension (1 wt%) and nanocrystalline cellulose (NCC) aqueous suspension (11 wt%) were purchased from Cellulose Lab. Microfibrillated cellulose (MFC) aqueous suspension (2.06 wt%) (see Figure 2.1a) was kindly supplied by Mid Sweden University (Sweden). All the cellulose suspensions display a gel-like behavior. NFC was refined with an homogenization process and shows particles with a wide range of diameters from micrometer to tens of nanometers and a length of several micrometers, as shown in Figure 2.1b. It presents a web-like structure with a extensive hydrogen-bonding ability and a high surface area. Tempo NFC exhibits a diameter between 4 nm and 20 nm and a length ranging from 500 to 2000 nm. NCC has a crystallinity of 87% with a diameter between 3 nm and 5 nm and a length comprised between 90 nm and 300 nm. For both Tempo NFC and NCC, the particles are too small to be resolved from optical microscope, therefore no defined features can be observed in Figure 2.1c and 2.1d.

2.2. Substrate preparation

Polystyrene-block-poly(ethylene-ran-butylene)-block-polystyrene (SEBS) Tuftec H1062 was dissolved in toluene with a content of 180mg/ml and stirred for 24 hours on a magnetic stirrer to obtain a gel-like solution. It was then dropcasted on a glass slide already cleaned with deionized water and dried with nitrogen. Once all the solvent was evaporated the substrate shown in

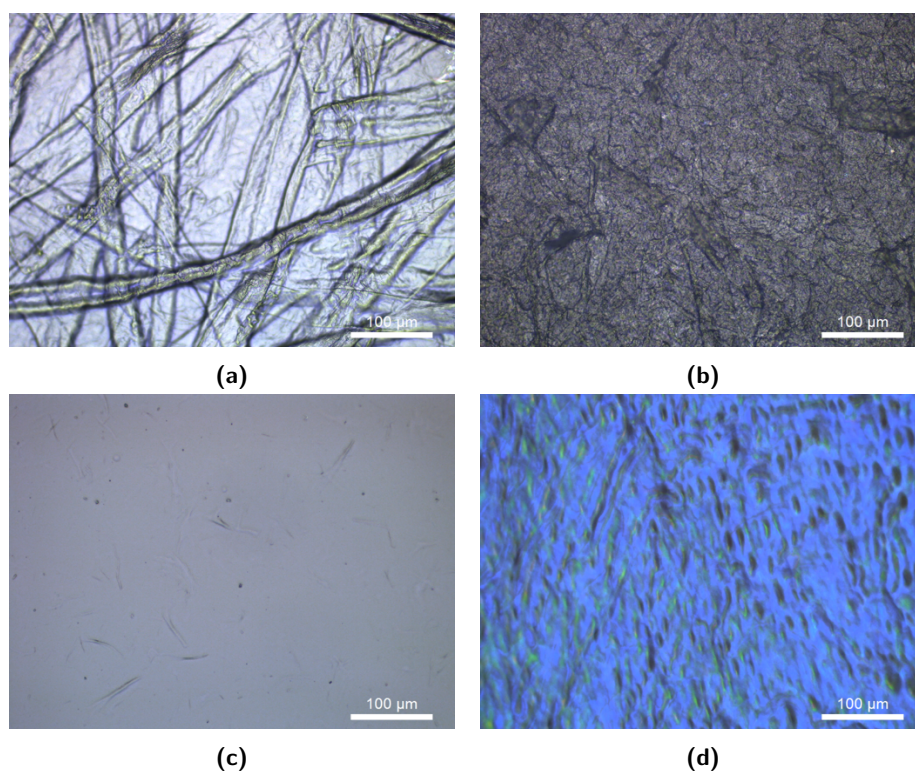


Figure 2.1: Optical microscope pictures of dropcasted film made by: (a) MFC, (b) NFC, (c) Tempo NFC, (d) NCC.



Figure 2.2: SEBS substrate after evaporation.

Figure 2.2 was obtained.

2.3. Printing

The cartridges used in this work have a capacity of up to 1.5 ml and a drop volume of 10 picoliter nominal, with a size nozzle of 21 μm . As discussed in the section 1.4, the particles dispersed in the ink should be $1/100^{\text{th}}$ the nozzle diameter to prevent clogging. Therefore the ink was filtered with a 0.2 μm nylon filter prior to filling the cartridge. To homogeneously print it is important to remove all the air bubbles inside the cartridge, reason for which the latter was placed in a vacuum desiccator for 2 hours.

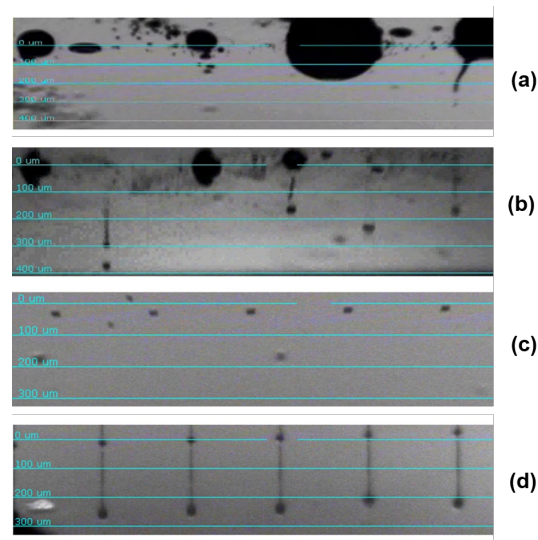


Figure 2.3: Typical jetting behaviours observed by the drop watcher: (a) clogging, (b) misfiring, (c) nonjetting, (d) stable jetting. Adapted from [59]

Before proceeding with printing, a second cartridge filled with deionized water was installed in the printer to check the proper jetting of each nozzle through the drop watch camera (see Figure 1.13a). Clogging, misfiring and nonjetting are the typical instabilities that may be observed while jetting[59]. Clogging is an extremely complex phenomenon caused by aggregation of small

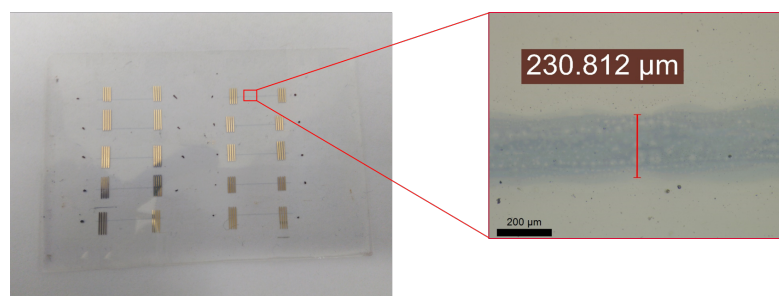


Figure 2.4: *PEDOT:PSS printed pattern on the transparent SEBS substrate, composed of 10 lines arranged in two columns, with gold electrodes. On the right, a magnified image of one single line taken with an optical microscope.*

particles at the nozzle entrance and the presence of impurities [60]. Figure 2.3a shows the typical jetting behavior observed by the drop watch camera in the described case. In order to remove those aggregated particles, two main procedures were performed. Firstly, the maximum voltage value was applied to the piezoelectric actuator in order to increase the pressure inside the ink supply. After that, the nozzles were purged with cleaning cycles. In case of heavy clogging, the cartridge was removed from the holder to gently wipe the head with a Cleanroom wipe soaked in deionized water. In case of misfiring, the jets have different directions with different velocities among the 16 nozzles, as shown in Figure 2.3b. It is important to correct this behavior in order to have the same working conditions for all the nozzles used simultaneously. The drop velocity can be adjusted by tuning the applied voltage to each nozzle, whereas the different directions can be corrected by prolonging the cleaning cycle. Nonjetting (see Figure 2.3c) can be due to a heavy clogging of the nozzles or a malfunction of the cartridge.

Once the proper operation of the nozzles, shown in Figure 2.3d, was achieved, the substrate was loaded on the platen (see Figure 1.13a) and fixed with vacuum. To increase the contrast between the substrate and the platen of the inkjet printer, the dropcasted SEBS substrate was transferred onto a silicon dioxide wafer. As detailed in the section 1.4, it is essential to activate the surface of the substrate before printing, in order to increase its surface energy. According to our experiment, a treatment with oxygen plasma for 20 seconds at 150 W was adequate to increase the surface energy more than the ink's surface tension, performed with a Technics Micro-RIE Series 800 Plasma. After that, the substrate was re-loaded on the printer platen in the same position and the alignment was performed.

As a last step the cartridge containing deionized water was removed from the printer and its head was installed onto the ink cartridge mounted into the printer. The jetting check procedure was repeated to verify the proper working of all the nozzles before printing the desired pattern. During printing, the cartridge was heated to 32°C, while the sample platen was set to 35°C. The drop-to-drop distance was set to 30 μm with 3 adjacent nozzles simultaneously used. The PEDOT:PSS pattern was obtained by using 15 layers consecutively printed. Figure 2.4 shows the obtained pattern printed on the SEBS substrate.

2.4. PEDOT:PSS/cellulose composite preparation

Cellulose nanoparticle suspension was mixed with PEDOT:PSS and the chosen additive (dimethyl sulfoxide (DMSO), glycerol, polyethylene glycol (PEG), ionic additives) with a high-shear mixer for 2 minutes at 10000 RPM, prior to be placed in a vacuum desiccator to remove the air bubbles.

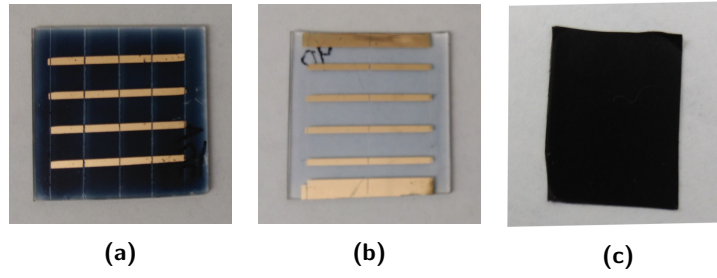


Figure 2.5: (a) *PEDOT:PSS/cellulose(1:1)* dropcasted film on glass substrate with gold electrodes (b) *PEDOT:PSS/cellulose(1:20)* dropcasted film on glass substrate with gold electrodes, (c) *PEDOT:PSS/cellulose(1:1)* free standing film.

Thick free standing films, shown in Figure 2.5c, were obtained by drying the mixture in a Teflon mold for 3 days, followed by annealing in oven at 70°C for additional 4 days.

Thin films were acquired by dropcasting the mixture onto a glass slide and drying for two days in ambient condition, followed by hot plate annealing at 130°C for 15 minutes. The same procedure was also performed on SiO_2/Si substrate, obtaining comparable results. Before casting, both glass and SiO_2/Si substrates were sonicated in acetone for 1 minute, then rinsed in 2-propanol and deionized water and blew dry with nitrogen gas. To improve the wettability of the substrate, the surface was further treated with oxygen plasma for 30 seconds at 150W prior to dropcasting. Figures 2.5b and 2.5a show the final films with gold electrodes on top of the surface.

To perform bending and stretching tests, the mixture was dropcasted onto a SEBS substrate, prepared as detailed in Section 2.2, and dried in ambient condition for 2 days. After that, the film was annealed at 80°C for 15 minutes.

2.5. Contact evaporation

In order to decrease the effect of the contact resistance and to have a homogeneous current density along the sample, 40 nm thick gold metal electrodes were thermally evaporated on the samples prepared as detailed in the previous sections. The process was carried out by using a shadow mask fixed to the samples by means of adhesive tapes. The alignment was performed manually.

The process was carried out with a thermal metal evaporator (see Figure 2.6a). A crucible containing the gold, shown in Figure 2.6b, was heated up with an electrical current of 20 A to melt the metal under 10^{-5} Torr vacuum. To prevent damage to the heat sensitive substrate (e.g. the SEBS substrate), the process was carried out with low rate equal to 0.3 nm/s.

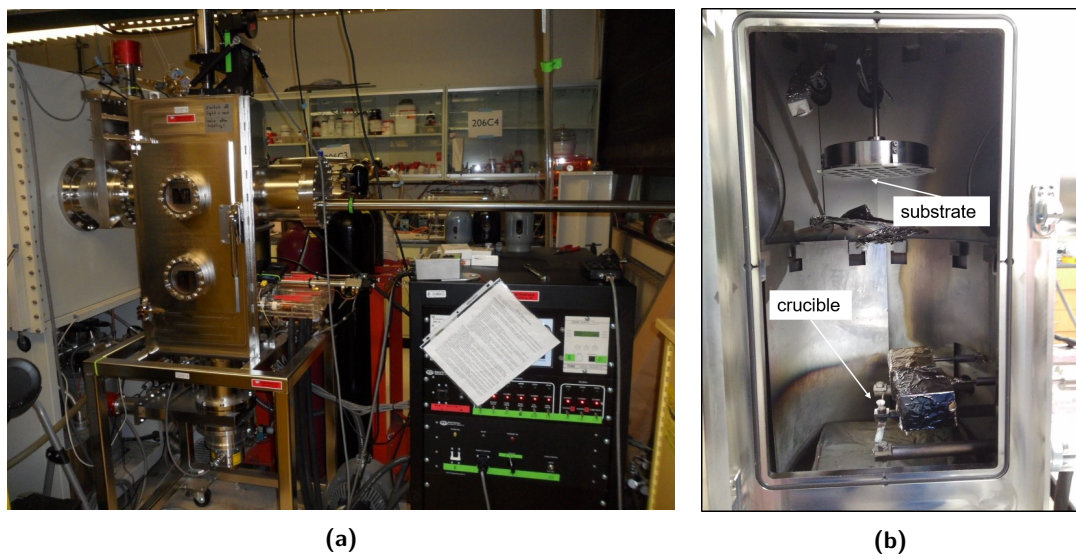


Figure 2.6: (a) Metal evaporator, (b) vacuum chamber.

3. Characterization

This chapter presents the equipments and the procedures employed to characterize the materials. The first two sections contain the measurements carried out to extract the conductivity from resistance and geometrical dimensions. The next section describes the humidity set-up used. The fourth part describes the stretching station employed to evaluate bending and stretching. The last section details surface tension and surface energy measurements.

3.1. Resistance evaluation

Electrical resistivity is an intrinsic property of a material which depends on the charge transport mechanism inside it. In case of a material with uniform section it is defined by:

$$\rho = \frac{Rwt}{l} \quad (3.1)$$

where R is the electrical resistance, w is the width, t is the thickness and l is the length. Therefore, by knowing the geometrical dimensions and measuring the electrical resistance, it is possible to evaluate the resistivity of the considered material. Conductivity can then be extracted from:

$$\sigma = \frac{1}{\rho} \quad (3.2)$$

The resistance of the PEDOT:PSS/cellulose composite films was measured with a Keithley 2400 source meter in ambient environment. Due to the low resistance of the films, a 4-points probe configuration was used to eliminate the contact resistance from the measurement.

For the PEDOT:PSS printed pattern, the small sizes of the evaporated electrodes required the use of a probe station in ambient environment connected to a Keithley 4200 characterization system. Due to the high aspect ratio of the printed pattern, the resulting resistance was high enough to be accurately evaluated in 2-points probe configuration. A gold nanowire soldered to the tip of each probe allowed to contact the soft sample with the utilized manipulator.

3.2. Morphological characterization

In order to extract the conductivity, the geometrical dimensions must be known. The length and the width of the PEDOT:PSS/nanocellulose composite films are determined by the distance between the electrodes and the sizes of the substrate, both known parameters. The width of the PEDOT:PSS printed pattern depends instead on the quality of the printing process and was evaluated with an optical microscope.

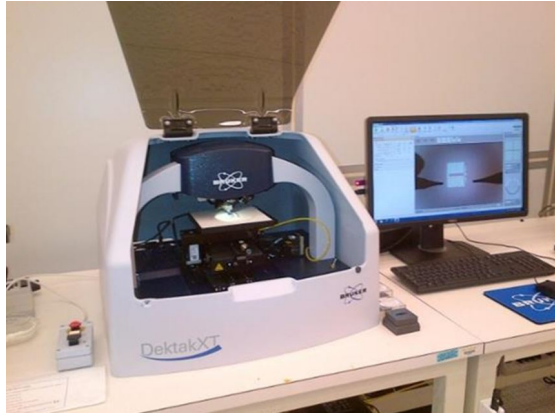
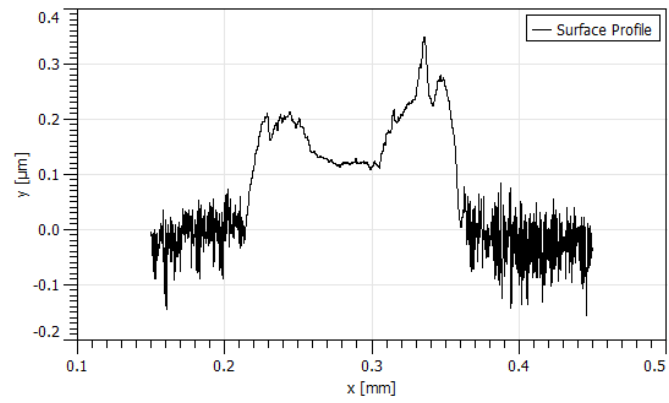
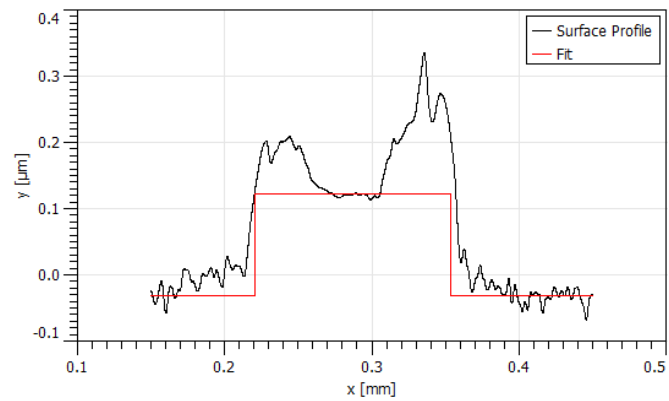


Figure 3.1: Bruker Dektak XT profilometer



(a)



(b)

Figure 3.2: (a) Typical surface profile of the PEDOT:PSS printed pattern on SEBS, (b) Profile after the post-process and fitting step function.

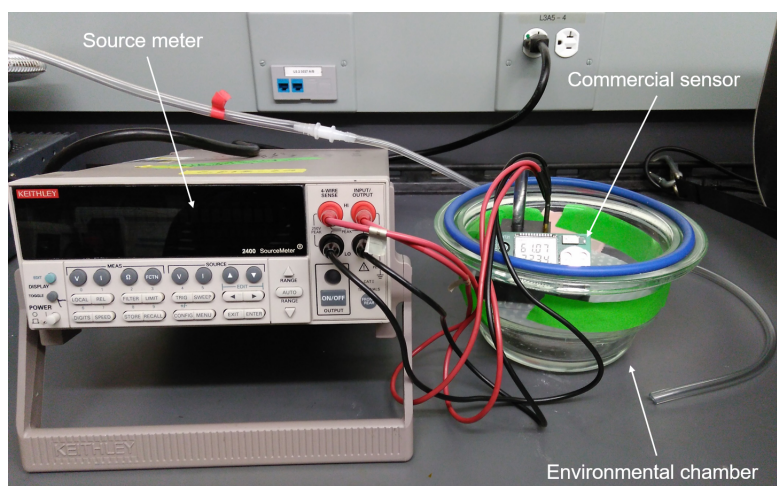


Figure 3.3: *Humidity measurement set-up*

Thickness of samples was measured using a Bruker Dektak XT profilometer (see Figure 3.1). For the samples on the glass substrate, the applied force was 5 mg, whereas the measurements for the PEDOT:PSS printed pattern required a force lower than 1 mg. Due to the high stickiness and the large surface roughness of SEBS, an additional post-process was carried out in the latter to extract the thickness. Figure 3.2a shows the acquired profile of a printed PEDOT:PSS line on the SEBS substrate. As first step, a low-pass filter was applied to remove the high-frequency noise, then the curve was fitted with a step function to extract the height, as shown in Figure 3.2b. To verify the obtained result, the measured height was compared with the one measured for the same pattern printed on a rigid SiO_2/Si wafer. The surface of the samples was further analyzed with a Veeco Multimode AFM in tapping mode.

3.3. Humidity measurements

The humidity measurement was carried out with the measurement set-up depicted in Figure 3.3 composed by a desiccator connected to a nitrogen pump used as home-made environmental chamber, a Keithley 2400 sourcemeter to read the electrical response and a commercially available SHT31 humidity and temperature sensor from Sensirion as reference. The humidity value inside the chamber was varied by tuning the amount of air flowing inside it due to desiccation and moistening processes. However, once the humidity inside the chamber reached the value of the external environment, the speed of the process was drastically reduced. A glass with sufficient amount of water was so introduced inside the chamber to speed up the process above this value. The sample was connected to the source meter positioned outside the chamber through four cables, as so to perform a 4 probes measurement of the electrical resistance. The reference sensor allowed to precisely read the humidity and the temperature value inside the chamber.

3.4. Mechanical Measurements

Mechanical measurements were performed with a home-built stretching station controlled with a LabView Virtual Instrument (VI), which allows to combine the stretching data with the elec-

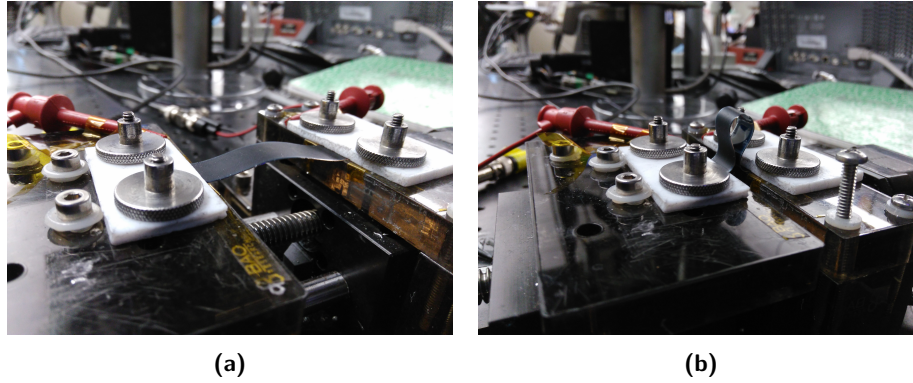


Figure 3.4: Sample mounted on stretching stage under bending test: (a) Initial position, (b) After bending.

Table 3.1: Polar and dispersive components of the surface tension of selected liquids used to extract substrate's surface free energy.

	$\gamma_L^p (mJ/m^2)$	$\gamma_L^d (mJ/m^2)$	$\gamma_L (mJ/m^2)$
chloroform	27.2	0	27.2
ethylene glycol	29	19	48
water	22.1	50.7	72.8
hexadecane	27.5	0	27.5
diiodomethane	48.5	2.3	50.8

trical response acquired with an Agilent E4980A LCR meter. Figure 3.4a shows a unit under test mounted on the stretching stage, with the two electrodes connected to the LCR meter. The versatility of the equipment allowed to perform not only stretching test, but also bending measurements, as shown in Figure 3.4b.

3.5. Adhesion evaluation

An FTA200 tensiometer from First Ten Armstrong (see Figure 3.5) was used to measure the ink's surface tension and the SEBS substrate's surface energy, by means of the Owns-Wendt method and the pendant drop method, detailed in Section 1.4.

The Owns-Wendt method allows to extract the surface energy of a substrate by measuring the contact angle of different liquids with a known surface tension. The three quantities are indeed related by Equation 1.5, which can be solved by linear regression. To have a considerable number of points, the measurement was carried out with 5 different liquids with known polar and dispersive surface tension, detailed in Table 3.1.

For each liquid in Table 3.1, the micro-syringe was filled and under it a SEBS substrate, prepared as detailed in section 2.2, was loaded on the sample holder. A constant volume of a fluid droplet was then applied to the SEBS surface from the micro-syringe, in order to create a sessile droplet onto the substrate. The camera positioned in front of the sample holder and aligned with the substrate surface was used capture the droplet shape and to extract the contact angle as an average of three consecutive measurements.

On the contrary, the pendant drop method allows to extract the surface tension of a given

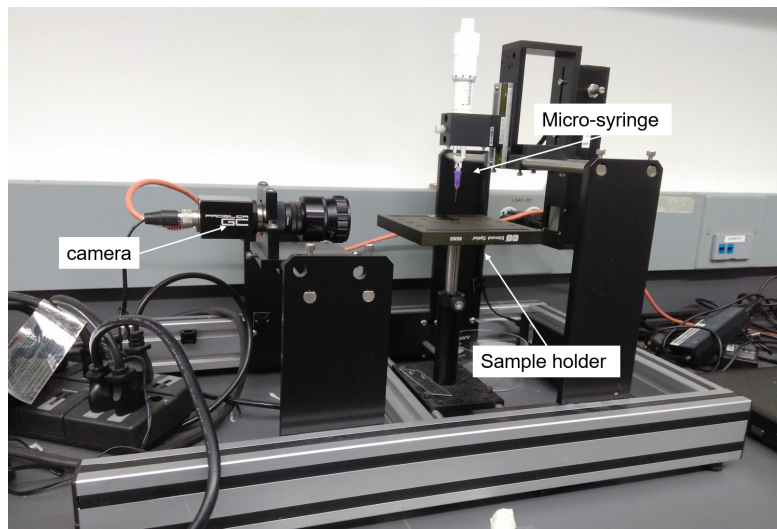


Figure 3.5: *Tensiometer from First Ten Angstroms.*

fluid by comparing the shape of a pendant drop with the theoretical value expected from the Young-Laplace equation 1.6. Prior to perform the measurement, the system was calibrated according to the size of the used needle (nominal diameter of 0.914 mm in our case). After that, the micro-syringe was loaded with the ink and a pendant drop was formed. The shape of the asymmetric drop was then captured with the camera and processed to extract the surface tension.

4. Inkjet printing of intrinsically stretchable PEDOT:PSS

This chapter describes electrical and mechanical properties of the printed PEDOT:PSS stretchable conductor. The first section discusses the additives used to optimize the ink, in order to obtain proper adhesion with the SEBS substrate and a good printability. The second section deals with the effect of the additives on the electrical conductivity. In the third section the resistance response to humidity is then presented. To investigate the effect of ionic additives on the humidity dependence, the resistance change in dependence of the relative humidity of a spincoated sample is discussed in the fourth section. The last section presents finally the stretchability of the inkjet printed conductor.

4.1. Surface activation

Electrical and mechanical properties of a printed device are highly affected by the adhesion between substrate and ink. As detailed in Section 1.4.2, the adhesion is mainly determined by two critical factors: the spreading of the ink onto the substrate and the coffee staining effect. The former can be controlled by adjusting the substrate's free energy and the ink's surface tension, while the latter is controlled by adding high-boiling point solvents such as DMSO.

Table 4.1: *Contact angle measured before and after surface plasma treatment.*

	contact angle before plasma(°)	contact angle after plasma(°)
chloroform	14.4 ± 0.3	13.0 ± 0.8
ethylene glycol	74.1 ± 0.6	56.4 ± 1.0
water	98.7 ± 0.5	74.9 ± 1.1
hexadecane	22.8 ± 1.2	6.9 ± 0.9
diiodomethane	43.9 ± 1.3	32.8 ± 0.9

Table 4.1 shows the measured contact angles onto SEBS of 5 different liquids with known surface tensions. The first column contains the values measured without any surface treatment, while the second column shows the results extracted after an oxygen plasma treatment of 20 seconds at 150W. By inserting these values in Equation 1.5, the y and the x components of the Owens-Wendt plot for each liquid are obtained, as shown in Figure 4.1 (for details see Section 1.4.2). A liner regression among all the values in the graph allows then to solve Equation 1.5 and to extract the polar and the dispersive component of the substrate's surface energy: the y-intercept relates to the dispersive component of the surface energy, whereas the slope

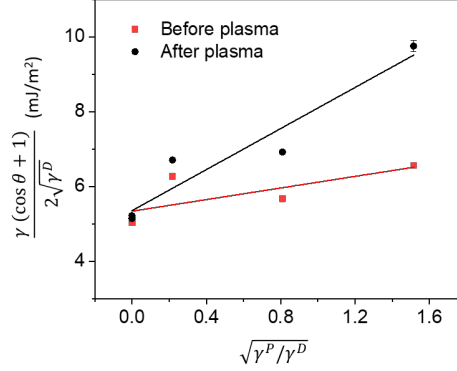


Figure 4.1: Owens-Wendt plot

is proportional to its polar component. Results in Table 4.2 prove that the performed plasma treatment increases the total surface energy by 7 mJ/m^2 , which indicates a higher wettability and an increased hydrophilicity of SEBS. These outcomes are in agreement with general observations that high surface energy leads to small wetting angle and large drop spreading [61].

Table 4.2: substrate's surface free energy before and after the surface treatment.

	$\gamma_L^p (\text{mJ/m}^2)$	$\gamma_L^d (\text{mJ/m}^2)$	$\gamma_L (\text{mJ/m}^2)$
Before plasma	0.60	28.55	29.15
After plasma	7.53	28.55	36.23

It can be noticed that the increase of total surface energy is caused only by the dispersive component, which suggests that the oxygen plasma treatment introduces polar functional groups into SEBS surface [62]. Due to the polar nature of water, it is attracted to these groups, resulting in a change of the surface properties of SEBS from being hydrophobic to hydrophilic.

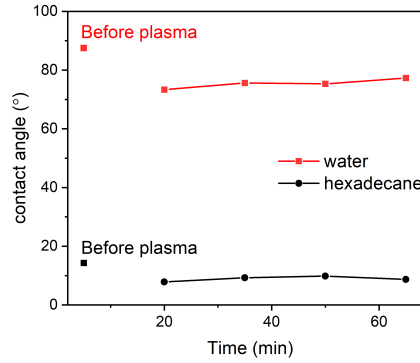


Figure 4.2: Hydrophobic recovery time after oxygen plasma treatment of SEBS substrate.

Figure 4.2 shows the recovery time of SEBS after oxygen plasma treatment. It can be noticed

that the measurement is not performed just after the plasma treatment, but rather a delay time of 20 minutes is considered. Time is indeed required before printing in order to perform alignment and jetting check procedures (see Section 2.3). The Table 4.3 shows that the contact angle of water droplets at 20 minutes is 16 % lower than the value measured before treatment, with a good stability within 65 minutes. The same trend can be observed for hexadecane, in which the contact angle measured at 20 minutes and 65 minutes varies of only 6 %. The outcome indicates that the SEBS retains the hydrophilicity acquired with the oxygen plasma treatment during the time period considered.

Table 4.3: *Percentage decrease of contact angles compared to the value measured before oxygen plasma treatment.*

	after 20 min (%)	after 65 min (%)
water	16	12
hexadecane	45	39

As detailed in Section 1.4.2, an optimal spreading over the substrate requires a surface tension of the ink lower than the substrate's surface energy. The surface tension of PEDOT:PSS water dispersion is known to be as high as 72.8 mJ/m^2 [63], almost double the substrate's surface energy previously measured. As shown by a previous work of our group [64], this value can be drastically reduced by adding a surfactant (10 wt%) to the ink solution. Table 4.4 shows the measured surface tension of the different developed PEDOT:PSS inks. It can be seen that the surface tension is highly affected by the addition of the surfactant, showing a value lower than the SEBS's surface energy previously measured. On the contrary, it does not show a notable dependence on the ionic additive content.

A previous study showed that addition of DMSO to PEDOT:PSS ink solution leads to a reduced coffee ring effect, a better resistance stability over one month and an increased conductivity [64]. However, Table 4.4 shows that the addition of DMSO results in an increase of the ink's surface tension by 2 mJ/m^2 , due to the surface tension of DMSO equal to 42 mJ/m^2 [65]. Despite that, the ink's surface tension with DMSO is still lower than the substrate's surface energy after the plasma treatment. Therefore all the developed inks shows an optimal surface tension value, which indicates a good adhesion with the substrate.

Table 4.4: *Surface tension of different compositions of PEDOT:PSS ink.*

Ink composition	$\gamma_L(\text{mJ/m}^2)$
PEDOT:PSS	72.8 [63]
PEDOT:PSS/STEC2(25 wt%)/Surfactant	31.6 ± 0.2
PEDOT:PSS/STEC2(25 wt%)/Surfactant/DMSO	33.2 ± 0.1
PEDOT:PSS/STEC2(50 wt%)/Surfactant/DMSO	33.7 ± 0.5
PEDOT:PSS/STEC1(25 wt%)/Surfactant/DMSO	33.4 ± 0.7

Figure 4.3 shows the transient jetting of the developed PEDOT:PSS ink seen from the drop-watch camera. It can be noticed that the droplets have spherical shape without satellite droplets, confirming the printability of the ink.

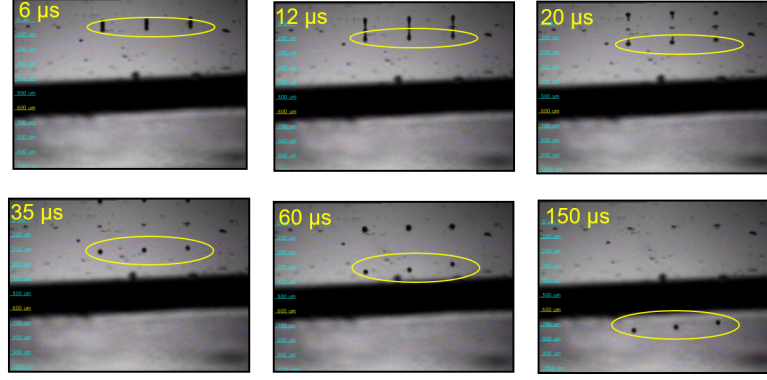


Figure 4.3: Jetting of optimized ink. Adapted from [64]

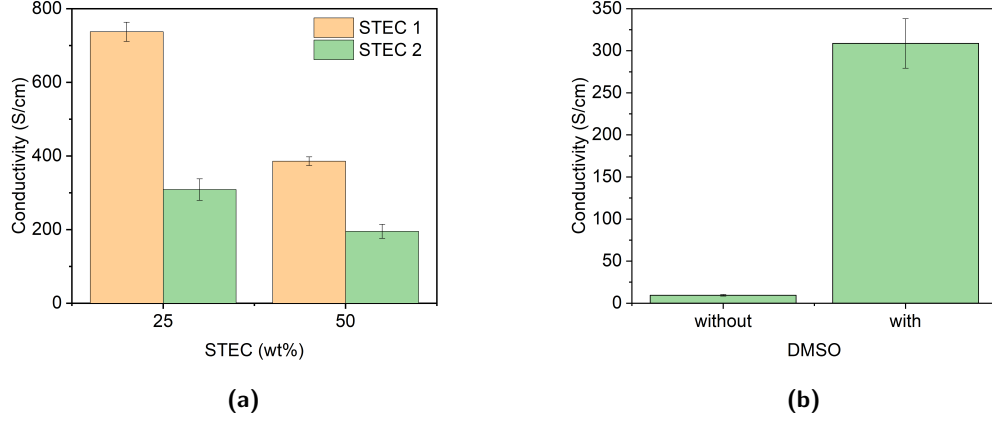


Figure 4.4: (a) conductivity for STEC1 and STEC2 as a function of ionic additive content, (b) conductivity for STEC1 with and without DMSO.

4.2. Conductivity

This section aims at studying the electrical performances of the inkjet-printed PEDOT:PSS/STEC conductor and the effects of additive on it. The printed feature for all the experiments is a simple line with the geometrical dimension detailed in Section 2.3. In order to have a consistent number of measurements, 10 lines are printed during the same printing session onto one SEBS substrate.

Figure 4.4a shows that doubling the ionic additive content leads to a notable decrease of conductivity, contrary to what observed in other works [7]. The same effect can be observed for both STEC1 and STEC2. The high content of surfactant is one possible reason responsible for the low conductivity measured at 50 wt% ionic additive. An increase of ionic additive content in the ink is expected to lead to height aggregation between PEDOT:PSS chains. To prevent it, a reduced content of PEDOT:PSS amount is used for the ink with 50 wt% ionic additive compared to 25 wt%. On the contrary, the content of surfactant in the ink is kept constant to obtain the same surface tension value. Therefore, the ration between the amount of surfactant and the amount of PEDOT:PSS decreases more than half from 25 wt% STEC to 50 wt% STEC.

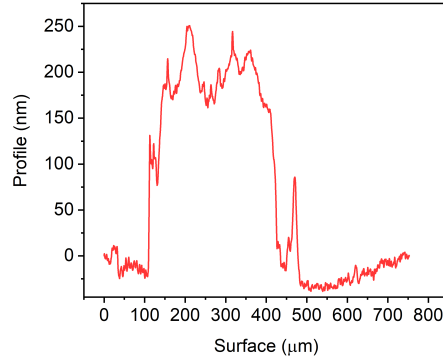


Figure 4.5: Profile of a printed feature without DMSO.

The printed feature thus contains a large amount of electrically insulating surfactant which limits the intra-chain hopping mechanism among PEDOT chains.

Furthermore, Figure 4.4a shows that the measured conductivity for STEC2 is two orders of magnitude higher than the expected value [7], which suggests an effect of the DMSO contained in the ink. DMSO is indeed a well known "secondary dopant" for PEDOT:PSS, able to enhance the conductivity more than 2 orders of magnitude, as discussed in Section 1.1.3. Figure 4.4b shows that the conductivity without DMSO decreases from about 308 S/cm to about 9 S/cm, which confirms our hypothesis. Moreover, the profile in Figure 4.5 shows a reasonable low coffee ring effect, which suggests that the DMSO removal does not lead to a degradation of the surface uniformity.

These outcomes suggest that the conductivity of a printed feature is highly affected by the surfactant and DMSO content: a large surfactant content leads to a high amount of insulating materials and a reduced conductivity, whereas the DMSO increases the conductivity of more than 2 orders of magnitude. On the contrary, the variation of ionic additive STEC2 content does not have a notable effect on the conductivity. For the purpose of this thesis, a printed conductor with low conductivity is required. Therefore the PEDOT:PSS ink with STEC2 and without DMSO is chosen for further investigations.

4.3. Humidity dependence

Figure 4.6a shows the resistance of the printed conductor with STEC2 and without DMSO under different humidity values within a time period of 3 hours. It can be noticed that the resistance follows the change of relative humidity without any significant delay time. At ambient condition ($\sim 45\%$ RH) a value of $70\text{ k}\Omega$ is measured, which increases up to $72.5\text{ k}\Omega$ at 0% RH. When the relative humidity is increased another time to 57% RH, the resistance drops of $7\text{ k}\Omega$. Nevertheless, when the relative humidity goes back to the initial value ($\sim 45\%$ RH), the resistance does not recover the initial value. To further investigate this behavior, a cycling measurement is carried out. The outcomes confirm the decrease of resistance proportionally to relative humidity, as shown in Figure 4.6b. However, a degradation of resistance at each cycle, due to an asymmetric behavior between humidification and drying process is observed.

Figure 4.7 shows the relative change of resistance as a function of relative humidity inside the chamber. It can be noticed that the resistance exhibits a linear behavior from 0% RH

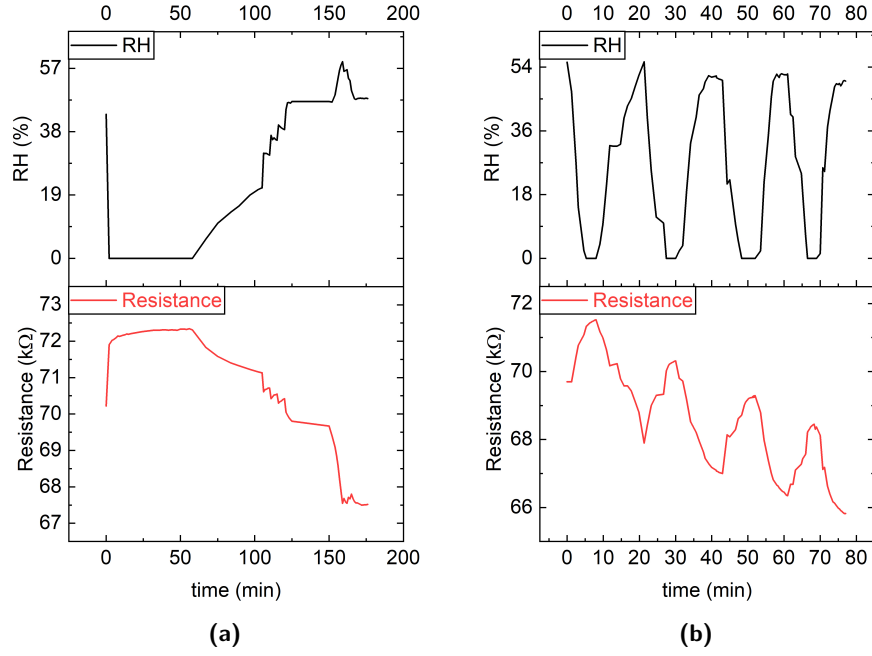


Figure 4.6: Humidity change and resistance response of printed PEDOT:PSS feature (a) for 1 cycle within 180 minutes (b) for 4 cycles within 80 minutes.

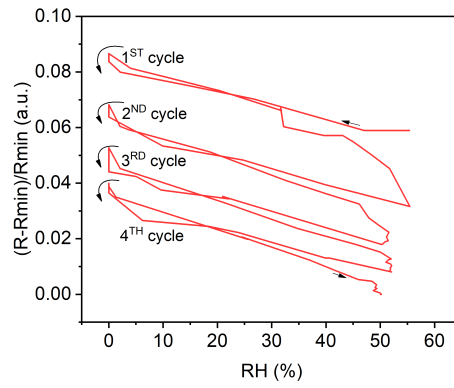


Figure 4.7: Change of relative resistance as a function of relative humidity.

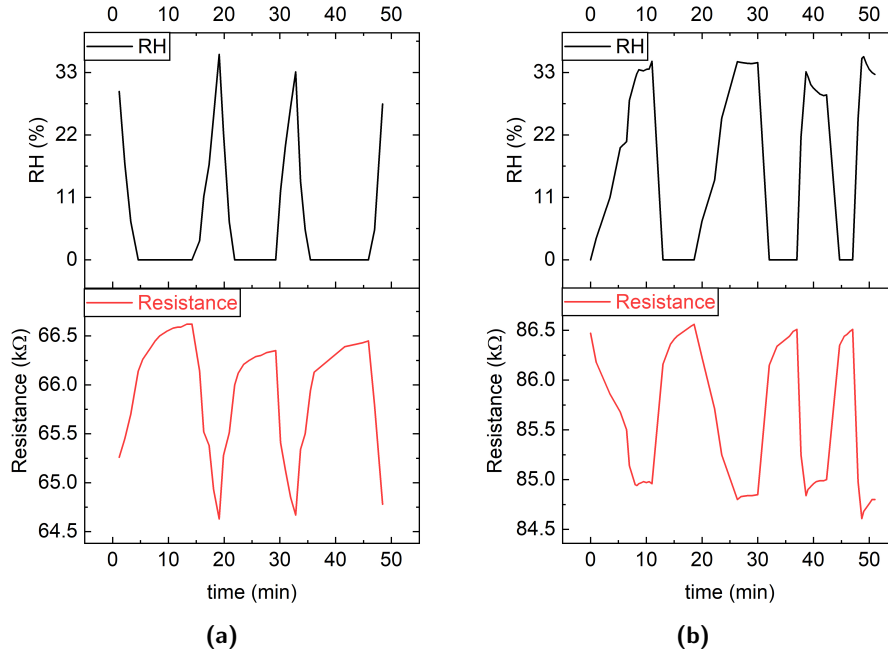


Figure 4.8: Humidity change and resistance response of printed PEDOT:PSS feature within 60 minutes (a) At ambient condition (b) after prolonged drying process of 12 hours.

to 40 % RH, with a good overlap between humidification and drying process. Once relative humidity exceeds this value, the resistance decays nonlinearly during humidification process, whereas a linear behavior can still be observed during drying process. Different studies observed a similar abrupt decrease of resistance in pristine PEDOT:PSS at ~ 80 % RH [66, 67]. Kuş and Okur showed that the phenomenon most probably originates by the saturation of water uptake inside PEDOT:PSS at 80 %RH, resulting in a water meniscus formed on the surface of the saturated PEDOT:PSS at higher relative humidity values [66]. Above saturation, ionic conductivity in water meniscus become then the predominant contribute to conduction, resulting in the observed resistance decrease.

Therefore, the measured trend seems to indicate that the addition of ionic additives lowers the saturation value of pristine PEDOT:PSS to 40 % RH. One possible reason responsible for the observed decrease of saturation point is the exchange of PSS protons by cations of ionic additives [68]. Water inside PEDOT:PSS is indeed directly adsorbed onto hydrophilic PSS sulfonic acid groups: $H_2O + PSS(HSO_3) \rightarrow H_3O^+ + PSS(SO_3)^-$ [67]. However, introduction of ionic additives onto PEDOT:PSS dispersion can lead to a replacement of cations of PSS sulfonic acid groups by organic cations of ionic additives. This exchange lowers the amount of hydrophilic PSS sulfonic acid groups available, resulting in a decreased sensitivity to humidity and a lower saturation value. Another possible explanation is the surfactant content in the ink, which is known to lower the bonds between PEDOT and PSS and to allow PSS to move more freely during solvent evaporation, leading to a phase separation between PEDOT and its counterion. The latter results in a reduced PSS content in the bulk layer and a lower amount of water uptake into it [69]. The effect of ionic additives and surfactant on the humidity response of PEDOT:PSS is further investigated in Section 4.4

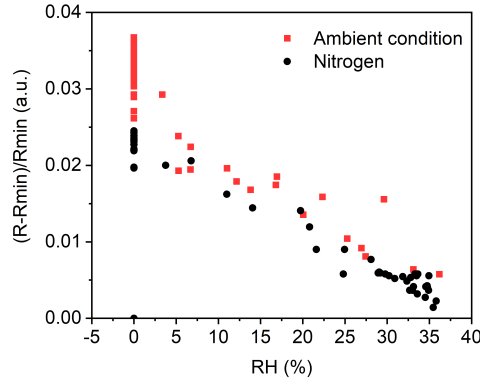


Figure 4.9: Change of relative resistance as a function of relative humidity.

To prove the linear behavior observed below saturation, a new cycling measurement is performed, as shown in Figure 4.8a. Resistance exhibits high stability among all the considered cycles with a reversible behavior between humidification and drying process. Figure 4.9 shows the linear dependence of the resistance with relative humidity, without notable hysteresis. To investigate the stability at low relative humidity, the device is exposed to low moisture level ($\sim 0\%$ RH) for several hours. Figure 4.8b shows the resistance and the relative humidity as a function of time after being dried for approximately 12 hours in a nitrogen dry box. The resistance verifies the trend observed in previous measurements, with a linear decrease as a function of relative humidity. Moreover, it confirms the high cycling stability and reversibility of humidification and drying process. On the other hand, it can be noticed that the absolute value of resistance after 12 hours drying increases by $20\text{ k}\Omega$ (see Figure 4.8b and 4.8a), which suggests a residual water content inside the polymeric matrix. The retention time at low humidity seems to be not sufficient enough for the adsorbed water above saturation to be able to diffuse out of the PEDOT:PSS polymer matrix.

This result indicate that the decrease of resistance above saturation is not an irreversible effect, but it can be recovered by a prolonged drying process.

4.4. Spincoating comparison

To decouple the effect of ionic additive and surfactant on the humidity response, PEDOT:PSS with only ionic additive (STEC2) is spincoated onto glass substrates. Figure 4.10 shows the resulting thickness as a function of RPM. As expected, the thickness decreases with RPM from 120 nm at 1000 RPM to 50 nm at 2000 RPM. A post-annealing step was performed at 80°C for 10 minutes.

Figure 4.11a shows the relative change in resistance as a function of relative humidity for different ionic additive content. It can be noticed that a low amount of ionic additive (20 wt%) highly improves the humidity sensitivity of pristine PEDOT:PSS, while a further increase result in the opposite effect. Moreover, at high ionic additive content (50 wt%), the resistance dependence becomes inversely proportional to relative humidity, as shown in Figure 4.11b.

The observed increase of resistance with humidity of pristine PEDOT:PS is in agreement with data in literature [30, 70]. Different studies shown that water molecules are adsorbed onto PSS sulfonic acid groups of the PSS rich-shell of PEDOT:PSS grain structure. The change in

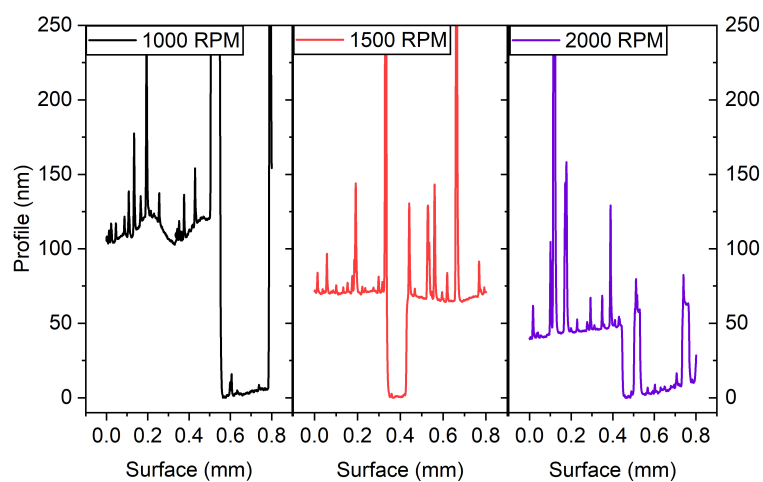


Figure 4.10: Extracted profile of spincoated PEDOT:PSS with STEC2 for different RPM.

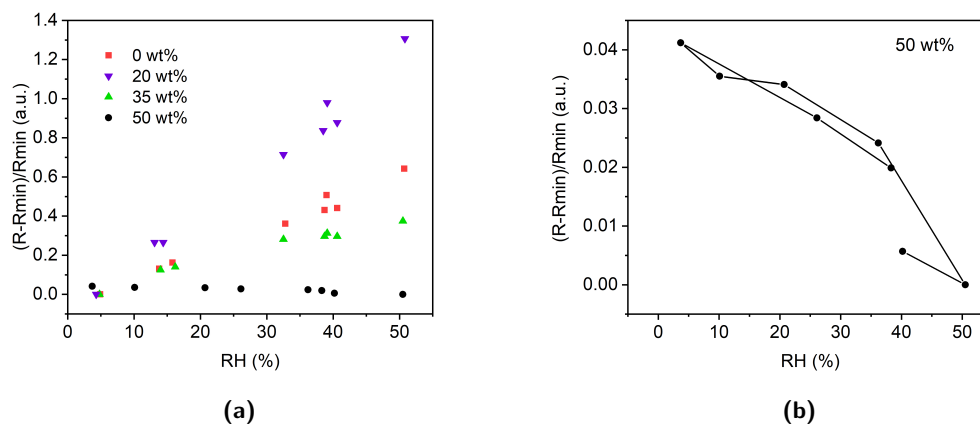


Figure 4.11: Relative resistance as a function of relative humidity of spincoated PEDOT:PSS with STEC2. (a) Different ionic additive content (b) magnified trend of 50 wt% STEC2.

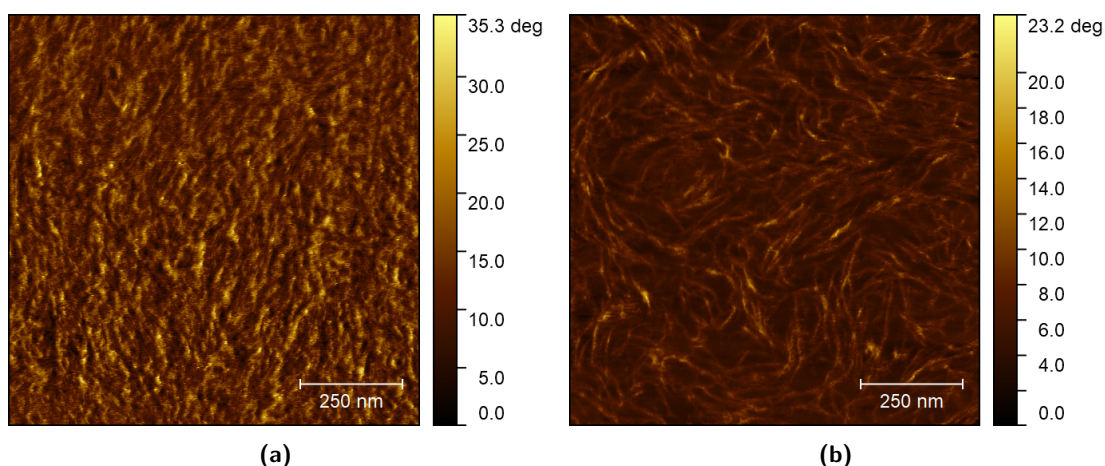


Figure 4.12: Phase AFM pictures of spincoated PEDOT:PSS with different content of STEC2: (a) 20 wt% (b) 50 wt%.

resistance is then dominated by two opposite effects, the decrease of mobility due to swelling of the film and the increase of mobility due to ionic conduction among water and PSS molecules [67]. In pristine PEDOT:PSS as well as PEDOT:PSS with ionic additive content of 20 wt% and 35 wt%, the process is dominated by the swelling effect, resulting in the observed resistance increase. As the AFM image in Figure 4.12a shows, a low ionic additive content does not affect the morphology of the film, in which the grain-structure of pristine PEDOT can still be clearly observed. Therefore, the adsorption of water onto the hydrophilic PSS is supposed to have the same effect observed in pristine PEDOT:PSS. The decreased sensitivity from 20 wt% to 35 wt% is consistent with previous literature [68].

On the contrary, AFM image for 50 wt % ionic additive (see Figure 4.12b) shows distinct nanofibrous structures, which suggest an alignment of PEDOT chains and a phase separation between PEDOT and PSS. Moreover Wang et al. demonstrated that the addition of STEC2 to PEDOT:PSS in a content higher than 40 wt% leads to an increased crystallinity of PEDOT, highly improving the intra-chain hopping mechanism and increasing the conductivity [7]. It follows that the PEDOT chains are no longer divided by the PSS-rich shell of the characteristic grains structure (see Figure 4.12a) but are aligned among them. Therefore the decrease of mobility due to swelling seems to be a negligible effect. Thus, the increase in mobility due to ionic conduction among water molecules in the PSS domain supposably becomes the dominant effect over resistance response to humidity. Moreover, the plot in Figure 4.11b confirms the low saturation at 40 % RH, which suggests that the observed behavior in the printed pattern is caused by the presence of ionic additives inside the ink instead of the surfactant.

4.5. Stretchability

Figure 4.13a shows the normalized resistance of printed PEDOT:PSS with a STEC2 (25 wt%) under increasing levels of strain. For low strain of 5 % and 10 %, the device exhibits approximate linear stretch-recovery curve. The resistance of recovery curve could almost return to the initial point after relaxing, which indicates an elastic deformation of printed pattern. When the latter is stretched to a higher strain as 15 %, 20 % and 25 %, a hysteresis phenomenon can be observed

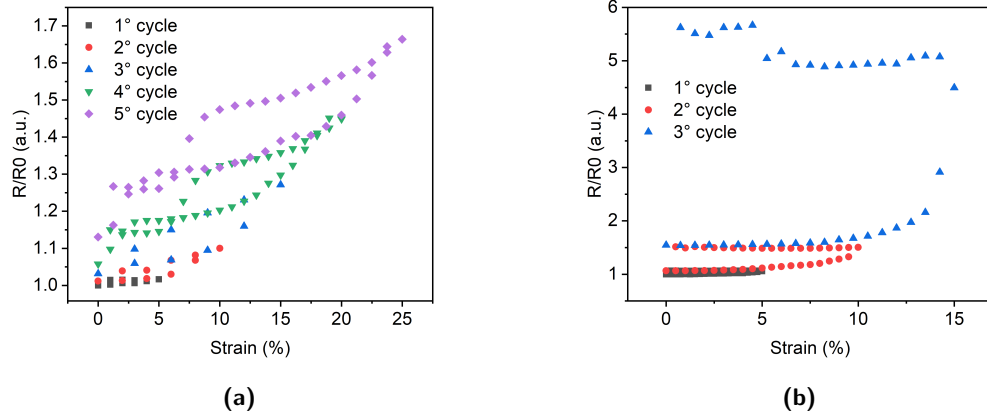


Figure 4.13: Normalized resistance under various strains for PEDOT:PSS with (a) 25 wt% STEC2, (b) 50 wt% STEC2.

between elongation and stress relaxation paths, with an increased resistance at the end of each cycle. Interestingly, we noticed that the original resistance value could be recovered when the sample is left to rest without stress within typically 1 hour, suggesting a slowly relaxing deformation mechanism. These outcomes indicate that printed PEDOT:PSS with a STEC2 content equal to 25 wt% can be stretched up to 25 wt% without a significant degradation of the electrical performance.

On the contrary the normalized resistance of PEDOT:PSS with a STEC2 content of 50 wt% shows an elastic behavior only at 5% of strain (see Figure 4.13b). At higher strain as 10 % and 15 % a significant difference can be observed between elongation and stress relaxation curves, leading to a final resistance notably larger than the initial value. One possible reason responsible for the large hysteresis is the formation of cracks along the printed PEDOT:PSS, which indicates a poor stretchability. The outcome suggest that the high content of surfactant compared to PEDOT:PSS has a degrading effect not only on the electrical performances as shown in the Section 4.2 but also on the mechanical properties.

5. Highly conductive PEDOT:PSS/cellulose composite

This chapter aims at presenting electrical and optical properties of the developed PEDOT:PSS/cellulose composite. The first section describes the correlation between cellulose nanoparticle and conductivity of the composite. The effects of different additives on the electrical performances of the composite are then discussed in the second section. The third section deals with the current transport mechanism. The last section shows the influence of cellulose nanoparticles on optical properties .

5.1. Influence of cellulose nanoparticles on conductivity

Figure 5.1a shows the electrical conductivity of the dropcasted PEDOT:PSS/nanocellulose films. The composite is made from the PEDOT:PSS aqueous suspension mixed with STEC1(6 vol%), further blended with cellulose nanoparticles. As expected, the conductivity decreases with the cellulose content. Nanofibrillated cellulose (NFC) composite exhibits the highest conductivity value among those, whereas Tempo-oxidize nanofibrillated cellulose (Tempo NFC) composite and nanocrystalline cellulose (NCC) composite show the lowest conductivity. It can be further noticed that a low addition of NFC (10 wt%) does not affect the conductivity of pristine PEDOT:PSS, while the same amount of Tempo NFC and NCC decreases the conductivity by around $1/3^{th}$.

The optical microscope images in Figure 5.1b show the surface of the dropcasted film (50 wt% of cellulose). As analyzed in Section 2.1, the MFC film consists of large fibers with a diameter of the order of micrometer, the NFC film consists of small and large fibers with a diameter ranging from nanometers to micrometers, while Tempo NFC and NCC films exhibit particles of the order of nanometers. It is therefore not surprising to notice the same features on the surface of the composite films: large fibers can be observed in both NFC and MFC films, whereas the surface of Tempo NFC and NCC exhibits high uniformity and low roughness. This observation is further verified by the measured surface roughness in Table 5.1.

Therefore, results in Figure 5.1a suggest a correlation between cellulose nanoparticles size and the resulting conductivity of the composite films, in agreement with other works [71]. It is supposed that small cellulose nanoparticles as Tempo NFC and NCC can create a film-like structure, reducing the contact between PEDOT:PSS conductive grains and affecting the overall conductivity. On the contrary, MFC and NFC form a web-like structure by which PEDOT:PSS grains are only partially separated. Thus the conductivity does not decrease as much as Tempo NFC and NCC. Other works in literature hypothesized an interaction between the hydroxyl groups (-OH) of cellulose with SO_3H groups of PSS, by which the conducting PEDOT:PSS forms an homogeneous coating around cellulose nanoparticles [13, 14]. In such a model, the

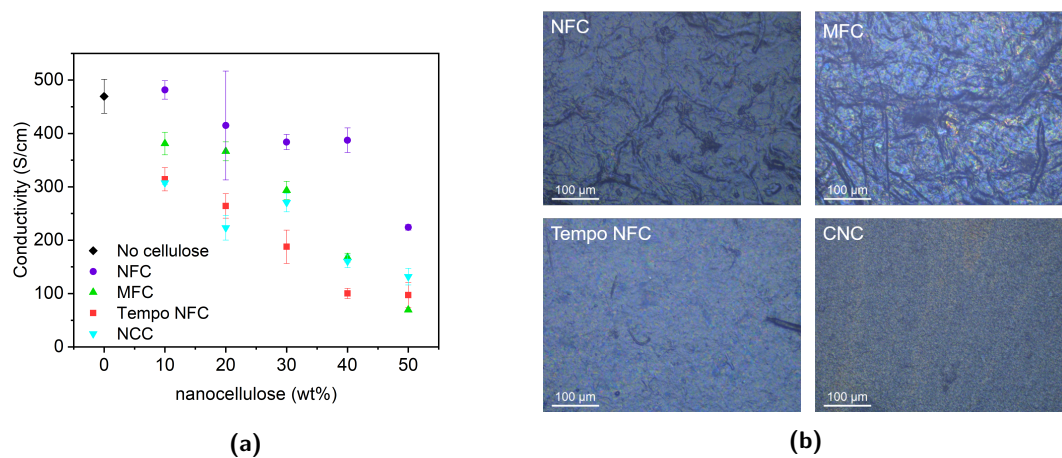


Figure 5.1: (a) Conductivity of PEDOT:PSS/cellulose composite as a function of cellulose content for different cellulose nanoparticles, (b) optical microscope pictures for different cellulose nanoparticles at 50 wt%.

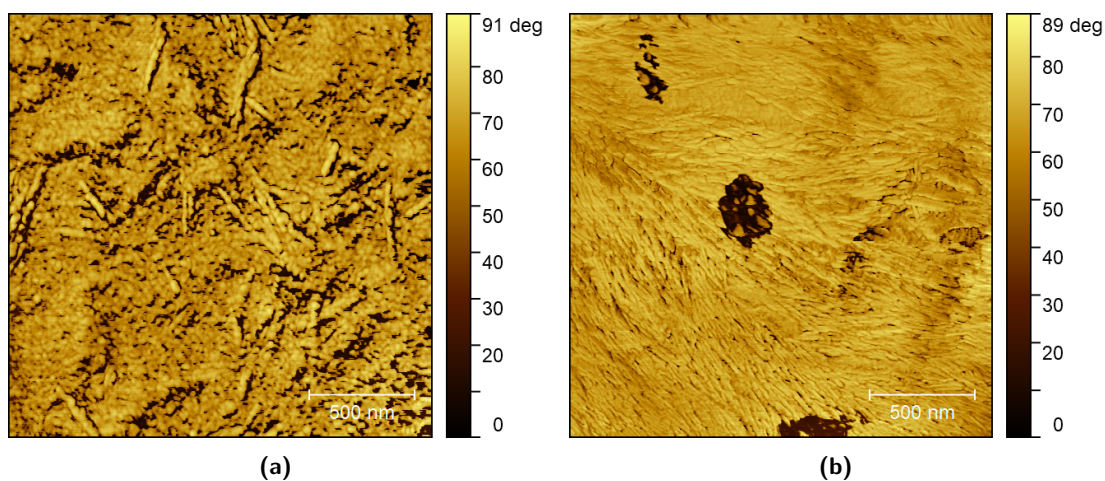


Figure 5.2: Phase AFM pictures for PEDOT:PSS/cellulose composite with (a) 10 wt% NCC (b) 50 wt% NCC.

Table 5.1: *Roughness average of PEDOT:PSS/cellulose dropcasted film for the 4 different cellulose nanoparticles.*

cellulose nanoparticle	Ra (μm) 10 wt%	Ra (μm) 20 wt%	Ra (μm) 30 wt%	Ra (μm) 40 wt%	Ra (μm) 50 wt%
NFC	0.556	0.654	0.799	0.815	0.985
MFC	0.709	1.034	1.232	2.310	2.700
Tempo NFC	0.160	0.202	0.216	0.213	0.225
NCC	0.165	0.105	0.134	0.144	0.159

long fibrils of NFC provide a structure around which PEDOT:PSS chains are aligned. On the contrary the alignment in Tempo NFC and NCC is expected to be lower due to the reduced dimension of the constituent nanoparticles affecting the resulting conductivity of the film. The precise mechanism is still under investigation.

Figure 5.2a shows the AFM image of the NCC composite (10 wt%). It can be noticed that the film is composed by small grains (PEDOT:PSS) and elongated nanoparticles (NCC). On the contrary in the AFM image of NCC composite with 50 wt% shown in Figure 5.2b, only nanoparticles with high aspect ratio can be observed. It suggests that at 10 wt% most of the PEDOT:PSS grains are not covered by NCC, resulting in a small decrease of conductivity compared to pristine PEDOT:PSS value, while at 50 wt% the amount of NCC is high enough to create the film-like structure, leading to the high decrease of conductivity observed in Figure 5.1a.

The I V curves in Figures 5.3a, 5.3b, 5.3c and 5.3d confirm that the current transport mechanism in the composite for all the cellulose nanoparticles is dominated by ohmic contribution.

5.2. Conductivity enhancement

The conductivity of composite made with NFC shows the highest value among the different cellulose nanoparticles. Therefore, we chose this composite with a cellulose content equal to 50 wt% for further investigations.

As first step, a study of the STEC1 content effect on the conductivity of composite is performed. In order to improve the conductivity, also DMSO, a well known “secondary dopants” for PEDOT:PSS (see Section 1.1.3), is added to the composite in the amount of 30 vol%. Results in Figure 5.4 show a negligible effect of STEC1 variation on the conductivity, with a change between the highest and the lowest values of only 27 %, which suggests a masking effect of DMSO over the conductivity enhancement effect of STEC1. Figure 5.5 shows thus the conductivity measured as a function of DMSO content in the composite, without STEC1. Without any additive, the composite exhibits a low conductivity of about 1 S/cm, comparable with the one of pristine PEDOT:PSS. The value is dramatically increased up to about 304 S/cm at a DMSO content of 10 vol%. Additional increase of DMSO slightly augments the conductivity up to about 401 S/cm at 50 vol% of DMSO. Figure 5.5 also shows that dropcasted and spincoated (500 RPM for 1 minute) films exhibit a comparable value of conductivity.

These outcomes prove that the addition of DMSO leads to a higher conductivity compared to STEC1. Moreover the combination of the two additives does not result in a significant increase of the conductivity.

To further study the conductivity dependence on different additives, glycerol and polyethylene glycol (PEG), two solvents known to improve PEDOT:PSS conductivity, are introduced in the composite doped with DMSO (50 vol%), in place of STEC1. Figure 5.6b shows a slightly increase

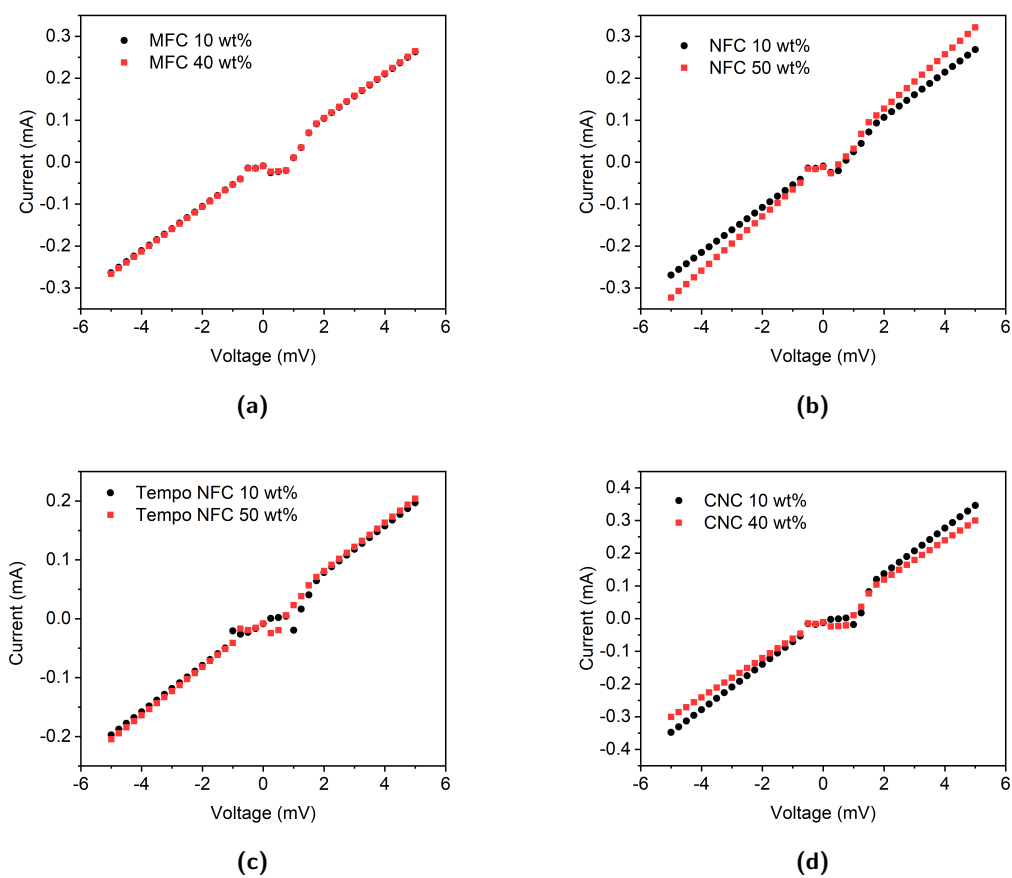


Figure 5.3: IV curves of PEDOT:PSS/cellulose composite for (a) MFC (b) NFC (c) Tempo NFC (d) NCC.

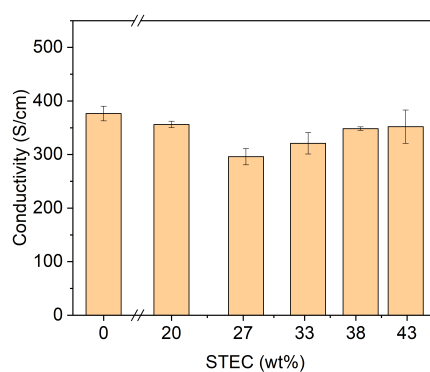


Figure 5.4: Conductivity of PEDOT:PSS/cellulose composite as a function of STEC content

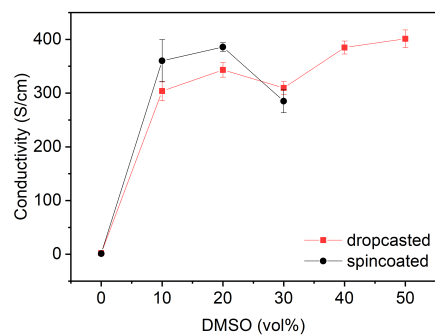


Figure 5.5: Conductivity of PEDOT:PSS/cellulose composite as a function of DMSO content.

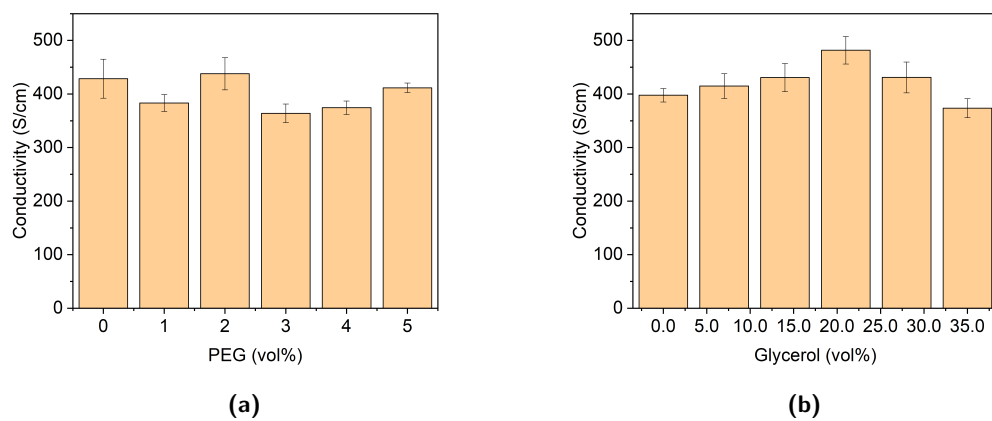


Figure 5.6: Conductivity of PEDOT:PSS/cellulose composite as a function of (a) Glycerol content, (b) PEG content.

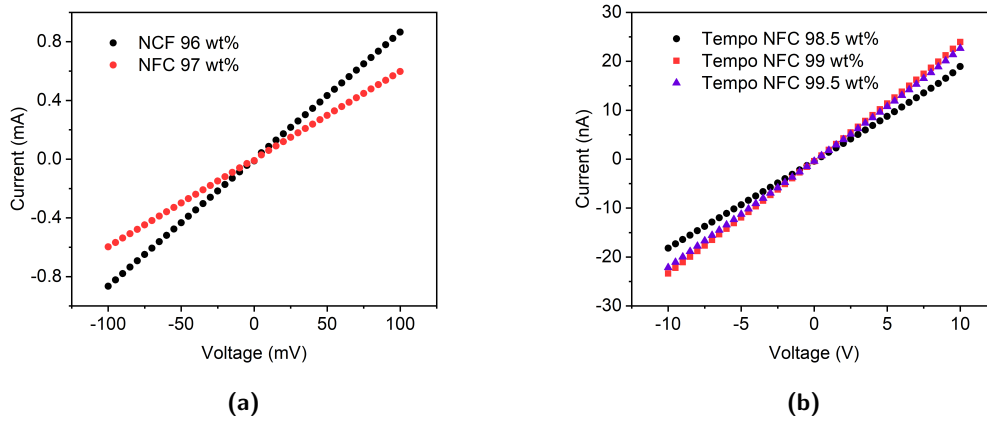


Figure 5.7: *IV curve of PEDOT:PSS/cellulose composite with (a) NFC (b) Tempo NFC.*

of the conductivity with glycerol content, with a maximum at 20 vol%, in agreement with other works. On the contrary, the conductivity as function of PEG content (molecular weight 200) does not show a significant change. These outcomes verify the DMSO masking effect observed for STEC1 on the conductivity enhancement process.

5.3. Percolation in the PEDOT:PSS/cellulose composite

In order to better understand the conduction mechanism in the composite doped with DMSO (50 vol%), the conductivity at high cellulose content is investigated. Following the results in Section 5.1, the study is performed on Tempo NFC-based composite and NFC-based composite. Figures 5.7a shows the I-V curves of the NFC composite with a cellulose content equal to 96 wt% and 97 wt%. The observed linear trend indicates a current transport mechanism dominated by ohmic contribution. Figure 5.7b shows that the same trend can be noticed for Tempo NFC composite (98.5 wt%, 99 wt% and 99.5 wt%), which suggest a negligible effect of tunneling contribution in relation to the current mechanism.

Figure 5.8 depicts the conductivity as a function of the cellulose content from 60 wt% to 99.5 wt%. The blend made with NFC shows a conductivity decay of 3 order of magnitudes from about 334 S/cm at 60 wt% to about 0.099 S/cm at 99.5 wt%. The same cellulose variation in the Tempo NFC composite results in a decay of more than 6 orders of magnitude, from about 163 at 60 wt% to about 3 μ S/cm at 99.5 wt%. This result confirms the conductivity dependence on the nanoparticles size observed in Section 5.1. Moreover, both composite exhibit an exponential decay of the conductivity as a function of the cellulose content with a sharp decrease above 95 wt%, which suggests a conduction mechanism based on percolation.

The conductivity trend above 95 wt% is further investigated, as shown in Figures 5.9b and 5.9a. Tempo NFC-based composite shows a plateau above 98.5 wt% (see Figure 5.9b). According to percolation theory, this value defines the percolation threshold, in which the composite changes from conductor to insulator. On the contrary NFC-based composite does not show any insulating behaviour in the range considered, as shown in Figure 5.9a.

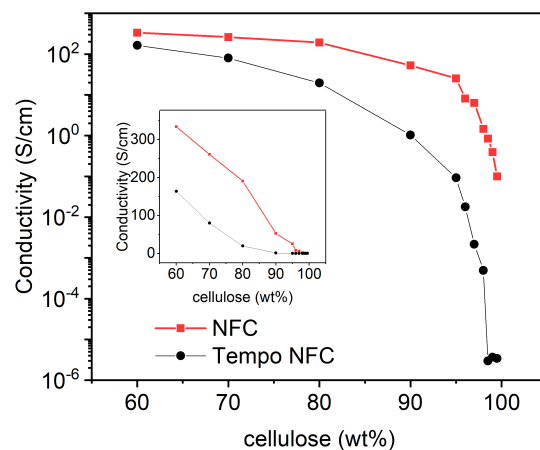


Figure 5.8: Conductivity of PEDOT:PSS/cellulose (NFC and Tempo NFC) composite as a function of cellulose from 60 wt% to 95 wt % in logarithmic and linear scale (small graph).

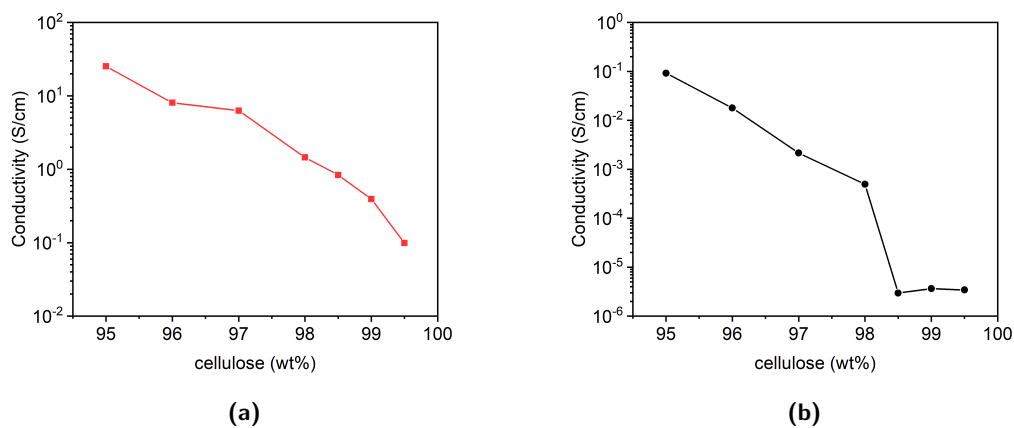


Figure 5.9: Conductivity of PEDOT:PSS/cellulose (NFC and Tempo NFC) composite as a function of cellulose: (a) from 95 wt% to 99.5 wt% of NFC; (b) from 95 wt% to 99.5 w% of Tempo NFC.

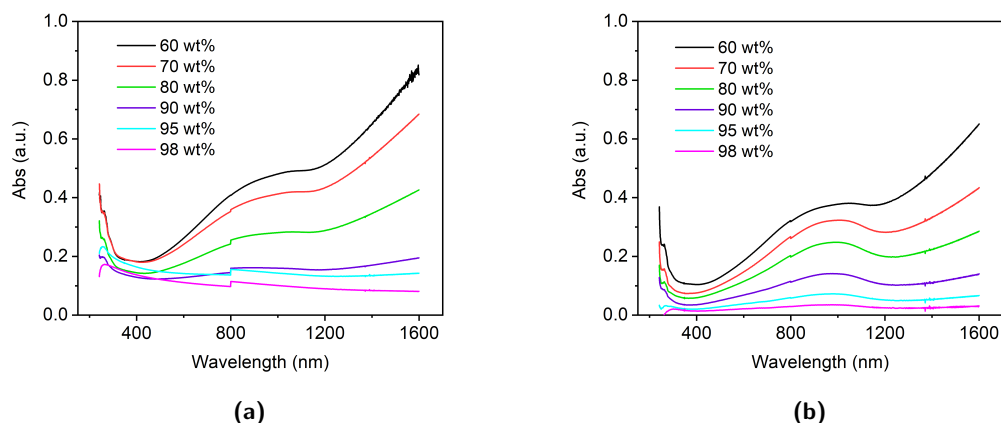


Figure 5.10: UV-vis-NIR spectra of PEDOT:PSS composite with (a) NFC (b) Tempo NFC.

5.4. Influence of cellulose nanoparticles on transparency

Figure 5.10a shows the UV-vis-NIR spectrum of the NFC composite for different cellulose content. The absorbance for 60 wt% exhibits three peaks, one in UV associated with PSS and two in NIR, associated with polaron or bipolaron states of PEDOT [72]. The increase of NFC content in the composite gradually lowers those three peaks until the material turns transparent in NIR with an NFC content equal to 98 wt%. On the contrary, the absorbance at 400 nm is slightly affected by the cellulose content due to scattering of the light source off the cellulose fibrils.

Figure 5.10b shows the UV-vis-NIR spectrum of the Tempo composite for different cellulose content. The spectrum for 60 wt% shows the same trend observed in the NFC composite with three peaks at 300 nm, 900 nm and 1600 nm. The absorbance decreases proportionally with the Tempo NFC content. In contrast to what observed for NFC, the increase of Tempo NFC content reduces the absorbance over the entire spectrum, leading to a high transparency for a cellulose content higher than 95 wt%. The small sizes of Tempo NFC nanoparticles are indeed one order of magnitude lower than the wavelength in the considered range.

6. Conclusion

The presented work showed two approaches to overcome the mechanical limitations of PEDOT:PSS for the development of organic conductors. The first approach consisted on developing a PEDOT:PSS-based aqueous ink by adding ionic additives, followed by printing intrinsically stretchable features for humidity sensing application on a high stretchable SEBS substrate. The second approach focused on blending PEDOT:PSS water dispersion with cellulose nanoparticles to obtain a strong and stiff organic conductor.

6.1. Inkjet printing of intrinsically stretchable PEDOT:PSS

We successfully developed a process for inkjet printing of intrinsically stretchable PEDOT:PSS with ionic additives.

Regarding the adhesion between substrate and ink, contact angle measurements showed the efficiency of an oxygen plasma treatment of 20 seconds at 150 W to lower the SEBS hydrophobicity. Furthermore, pendant drop measurements showed that adding a surfactant with a content of 10 wt % to the ink led to a significant reduction of ink's surface tension. Both results proved the optimal spreading of the developed ink over the substrate and the good adhesion between them.

Then electrical and mechanical response of a printed feature was characterized. It showed a conductivity value ranging from 10 S/cm to 700 S/cm according to the ionic additive used and to the presence of DMSO in the ink. Moreover, a notable dependence of the conductivity with the surfactant content in the ink was observed, which suggests the existence of a trade-off between conductivity and surface tension. Further studies should be performed to investigate the optimal value of surfactant content.

The resistance of printed PEDOT:PSS stretchable conductor showed a dependence to humidity with good cycling stability and negligible response time. Unfortunately, the resistance response to humidity exhibited a low sensitivity of 4 % with a saturation point at 40 % RH, after which a non-linear behavior was observed. Further humidity characterization measurements showed a notable effect of ionic additives content on the resistive response of PEDOT:PSS: a low content of ionic additive (20 wt%) led to an improved humidity sensitivity, whereas a further increase (35 wt%) resulted in the opposite effect. At an ionic additive content equal to 50 wt%, the resistance response started to decrease with humidity, probably due to the change of morphology from a grains-like structure to a nanofibers-like structure and the increased crystallinity of PEDOT:PSS at ionic additive content higher than 50 wt %. The precise mechanism is still under investigation.

The stretchability of the printed PEDOT:PSS stretchable conductor was thus demonstrated.

Future works will be focused on understanding the underlying mechanism for the resistive response to humidity, in order to optimize the sensitivity to humidity sensing. Further investiga-

tions will be also performed on the surfactant content to improve conducting and stretchability without degrading the adhesion with the substrate.

6.2. Highly conductive PEDOT:PSS/cellulose composite

We successfully developed a protocol to blend PEDOT:PSS water dispersion with cellulose nanoparticles to obtain a highly conductive composite.

Electrical characterization measurements showed a large influence of cellulose nanoparticles type on the overall conductivity: composites made by small nanoparticles (Tempo NFC and NCC) showed a large decay of the conductivity with the cellulose content, in contrast with composites made by large nanoparticles (NFC and MFC), which exhibit a less step conductivity decrease with cellulose content.

The investigation of different secondary dopants showed a predominant effect of DMSO, which was able to enhance the conductivity up to 430 S/cm at a cellulose content of 50 wt %. Additional additives did not show any notable effect on the conductivity of the composite. At low cellulose concentration, the composite exhibited a linear decrease with cellulose content, whereas for a cellulose concentration higher than 60 wt% an exponential decrease with the cellulose content was observed, which indicates a conduction mechanism based on percolation. The conductivity of the composite with small cellulose nanoparticles (Tempo NFC) showed a percolation threshold at a cellulose content equal to 98.5 wt%. On the contrary, the composite made with NFC did not show any insulating behavior up to 99.5 wt%.

Future works will focus on mechanical measurements. The influence of different cellulose nanoparticles, as well as the influence of different additives used to enhance the conductivity, on Young's Modulus and Tensile strength will be investigated. Further evaluation will be also carried out to evaluate the stability of conductivity to applied strains with bending and stretching tests.

Bibliography

- [1] M. Weiser, “The computer for the 21st century.” *Scientific American*, vol. 265, no. 3, pp. 94–104, 1991.
- [2] U. Hansmann, L. Merk, M. S. Nicklous, and T. Stober, *Pervasive computing handbook*. Springer Science & Business Media, 2013.
- [3] K. Ashton *et al.*, “That ‘internet of things’ thing,” *RFID journal*, vol. 22, no. 7, pp. 97–114, 2009.
- [4] G. P. Collins, “Next stretch for plastic electronics,” *Scientific American*, vol. 291, no. 2, pp. 74–81, 2004.
- [5] Y. Wen and J. Xu, “Scientific importance of water-processable pedot–pss and preparation, challenge and new application in sensors of its film electrode: A review,” *Journal of Polymer Science Part A: Polymer Chemistry*, vol. 55, no. 7, pp. 1121–1150, 2017.
- [6] K. Reuter, S. Kirchmeyer, and A. Elschner, “Pedot–properties and technical relevance,” *Handbook of Thiophene-Based Materials: Applications in Organic Electronics and Photonics*, pp. 549–576, 2009.
- [7] Y. Wang, C. Zhu, R. Pfattner, H. Yan, L. Jin, S. Chen, F. Molina-Lopez, F. Lissel, J. Liu, N. I. Rabiah *et al.*, “A highly stretchable, transparent, and conductive polymer,” *Science advances*, vol. 3, no. 3, p. e1602076, 2017.
- [8] S. Wagner and S. Bauer, “Materials for stretchable electronics,” *Mrs Bulletin*, vol. 37, no. 3, pp. 207–213, 2012.
- [9] D. J. Lipomi, J. A. Lee, M. Vosgueritchian, B. C.-K. Tee, J. A. Bolander, and Z. Bao, “Electronic properties of transparent conductive films of pedot: Pss on stretchable substrates,” *Chemistry of Materials*, vol. 24, no. 2, pp. 373–382, 2012.
- [10] J. Y. Oh, S. Kim, H.-K. Baik, and U. Jeong, “Conducting polymer dough for deformable electronics,” *Advanced Materials*, vol. 28, no. 22, pp. 4455–4461, 2016.
- [11] I. Hafez, H.-S. Yang, and W. T. Y. Tze, “Mechanically enhanced electrically conductive films from polymerization of 3, 4-ethylenedioxythiophene with wood microfibers,” *Journal of Applied Polymer Science*, vol. 134, no. 35, 2017.
- [12] K.-Y. Lee, Y. Aitomäki, L. A. Berglund, K. Oksman, and A. Bismarck, “On the use of nanocellulose as reinforcement in polymer matrix composites,” *Composites Science and Technology*, vol. 105, pp. 15–27, 2014.

- [13] M. Lay, M. À. Pèlach, N. Pellicer, J. A. Tarrés, K. N. Bun, and F. Vilaseca, "Smart nanopaper based on cellulose nanofibers with hybrid pedot: Pss/polypyrrole for energy storage devices," *Carbohydrate polymers*, vol. 165, pp. 86–95, 2017.
- [14] A. Malti, J. Edberg, H. Granberg, Z. U. Khan, J. W. Andreasen, X. Liu, D. Zhao, H. Zhang, Y. Yao, J. W. Brill *et al.*, "An organic mixed ion–electron conductor for power electronics," *Advanced science*, vol. 3, no. 2, p. 1500305, 2016.
- [15] H. Shirakawa, E. J. Louis, A. G. MacDiarmid, C. K. Chiang, and A. J. Heeger, "Synthesis of electrically conducting organic polymers: halogen derivatives of polyacetylene,(ch) x," *Journal of the Chemical Society, Chemical Communications*, no. 16, pp. 578–580, 1977.
- [16] C. K. Chiang, C. Fincher Jr, Y. W. Park, A. J. Heeger, H. Shirakawa, E. J. Louis, S. C. Gau, and A. G. MacDiarmid, "Electrical conductivity in doped polyacetylene," *Physical review letters*, vol. 39, no. 17, p. 1098, 1977.
- [17] S. Kirchmeyer and K. Reuter, "Scientific importance, properties and growing applications of poly (3, 4-ethylenedioxythiophene)," *Journal of Materials Chemistry*, vol. 15, no. 21, pp. 2077–2088, 2005.
- [18] G. Heywang and F. Jonas, "Poly (alkylenedioxythiophene) s—new, very stable conducting polymers," *Advanced Materials*, vol. 4, no. 2, pp. 116–118, 1992.
- [19] F. Jonas and G. Heywang, "De 3813589 (bayer ag)," *Prior: April*, vol. 22, 1988.
- [20] J. March, *Advanced organic chemistry: reactions, mechanisms, and structure*. John Wiley & Sons,, 1992.
- [21] L. Pauling, *The Nature of the Chemical Bond...* Cornell university press Ithaca, NY, 1960, vol. 260.
- [22] G. R. Strobl and G. R. Strobl, *The physics of polymers*. Springer, 1997, vol. 2.
- [23] R. E. Peierls and R. S. Peierls, *Quantum theory of solids*. Oxford University Press, 1955.
- [24] J. Brédas, B. Thémans, J. Fripiat, J. André, and R. Chance, "Highly conducting polypara-phenylene, polypyrrole, and polythiophene chains: An ab initio study of the geometry and electronic-structure modifications upon doping," *Physical Review B*, vol. 29, no. 12, p. 6761, 1984.
- [25] W. Li and H. Kwok, "Conduction mechanisms in organic semiconductors," in *Encyclopedia of Nanotechnology*. Springer, 2012, pp. 493–500.
- [26] V. Coropceanu, H. Li, P. Winget, L. Zhu, and J.-L. Brédas, "Electronic-structure theory of organic semiconductors: charge-transport parameters and metal/organic interfaces," *Annual Review of Materials Research*, vol. 43, pp. 63–87, 2013.
- [27] A. Lund, N. M. van der Velden, N.-K. Persson, M. M. Hamed, and C. Müller, "Electrically conducting fibres for e-textiles: An open playground for conjugated polymers and carbon nanomaterials," *Materials Science and Engineering: R: Reports*, vol. 126, pp. 1–29, 2018.
- [28] L. Vanmaele. Conducting polymer materials for flexible opv applications: Orgacon pedot:pss. [Online]. Available: <https://www.sigmaaldrich.com/technical-documents/articles/materials-science/organic-electronics/agfa-opv.html>

- [29] U. Lang, E. Müller, N. Naujoks, and J. Dual, “Microscopical investigations of pedot: Pss thin films,” *Advanced Functional Materials*, vol. 19, no. 8, pp. 1215–1220, 2009.
- [30] S. R. Dupont, F. Novoa, E. Voroshazi, and R. H. Dauskardt, “Decohesion kinetics of pedot: Pss conducting polymer films,” *Advanced Functional Materials*, vol. 24, no. 9, pp. 1325–1332, 2014.
- [31] T. Stöcker, A. Köhler, and R. Moos, “Why does the electrical conductivity in pedot: Pss decrease with pss content? a study combining thermoelectric measurements with impedance spectroscopy,” *Journal of polymer science part B: polymer physics*, vol. 50, no. 14, pp. 976–983, 2012.
- [32] J. Kim, J. Jung, D. Lee, and J. Joo, “Enhancement of electrical conductivity of poly (3, 4-ethylenedioxythiophene)/poly (4-styrenesulfonate) by a change of solvents,” *Synthetic Metals*, vol. 126, no. 2-3, pp. 311–316, 2002.
- [33] H. Shi, C. Liu, Q. Jiang, and J. Xu, “Effective approaches to improve the electrical conductivity of pedot: Pss: a review,” *Advanced Electronic Materials*, vol. 1, no. 4, p. 1500017, 2015.
- [34] A. MacDiarmid and A. J. Epstein, “The concept of secondary doping as applied to polyaniline,” *Synthetic metals*, vol. 65, no. 2-3, pp. 103–116, 1994.
- [35] J. Ouyang, ““secondary doping” methods to significantly enhance the conductivity of pedot: Pss for its application as transparent electrode of optoelectronic devices,” *Displays*, vol. 34, no. 5, pp. 423–436, 2013.
- [36] N. Kim, S. Kee, S. H. Lee, B. H. Lee, Y. H. Kahng, Y.-R. Jo, B.-J. Kim, and K. Lee, “Highly conductive pedot: Pss nanofibrils induced by solution-processed crystallization,” *Advanced materials*, vol. 26, no. 14, pp. 2268–2272, 2014.
- [37] J. Y. Oh, M. Shin, J. B. Lee, J.-H. Ahn, H. K. Baik, and U. Jeong, “Effect of pedot nanofibril networks on the conductivity, flexibility, and coatability of pedot: Pss films,” *ACS applied materials & interfaces*, vol. 6, no. 9, pp. 6954–6961, 2014.
- [38] U. Lang, N. Naujoks, and J. Dual, “Mechanical characterization of pedot: Pss thin films,” *Synthetic Metals*, vol. 159, no. 5-6, pp. 473–479, 2009.
- [39] D. Qi, Z. Liu, W. R. Leow, and X. Chen, “Elastic substrates for stretchable devices,” *MRS Bulletin*, vol. 42, no. 2, p. 103–107, 2017.
- [40] —, “Elastic substrates for stretchable devices,” *MRS Bulletin*, vol. 42, no. 2, pp. 103–107, 2017.
- [41] G. Zheng, Y. Cui, E. Karabulut, L. Wågberg, H. Zhu, and L. Hu, “Nanostructured paper for flexible energy and electronic devices,” *MRS bulletin*, vol. 38, no. 4, pp. 320–325, 2013.
- [42] R. J. Moon, A. Martini, J. Nairn, J. Simonsen, and J. Youngblood, “Cellulose nanomaterials review: structure, properties and nanocomposites,” *Chemical Society Reviews*, vol. 40, no. 7, pp. 3941–3994, 2011.
- [43] H. Zhu, Z. Fang, C. Preston, Y. Li, and L. Hu, “Transparent paper: fabrications, properties, and device applications,” *Energy & Environmental Science*, vol. 7, no. 1, pp. 269–287, 2014.

- [44] M. A. S. Azizi Samir, F. Alloin, and A. Dufresne, "Review of recent research into cellulosic whiskers, their properties and their application in nanocomposite field," *Biomacromolecules*, vol. 6, no. 2, pp. 612–626, 2005.
- [45] Y. Nishiyama, G. P. Johnson, A. D. French, V. T. Forsyth, and P. Langan, "Neutron crystallography, molecular dynamics, and quantum mechanics studies of the nature of hydrogen bonding in cellulose $i\beta$," *Biomacromolecules*, vol. 9, no. 11, pp. 3133–3140, 2008.
- [46] Y. Nishiyama, P. Langan, and H. Chanzy, "Crystal structure and hydrogen-bonding system in cellulose $i\beta$ from synchrotron x-ray and neutron fiber diffraction," *Journal of the American Chemical Society*, vol. 124, no. 31, pp. 9074–9082, 2002.
- [47] Y. Nishiyama, "Structure and properties of the cellulose microfibril," *Journal of Wood Science*, vol. 55, no. 4, pp. 241–249, 2009.
- [48] S. Eichhorn and G. Davies, "Modelling the crystalline deformation of native and regenerated cellulose," *Cellulose*, vol. 13, no. 3, pp. 291–307, 2006.
- [49] H. Zhu, W. Luo, P. N. Ciesielski, Z. Fang, J. Zhu, G. Henriksson, M. E. Himmel, and L. Hu, "Wood-derived materials for green electronics, biological devices, and energy applications," *Chemical reviews*, vol. 116, no. 16, pp. 9305–9374, 2016.
- [50] H. Meier, "Chemical and morphological aspects of the fine structure of wood," *Pure and applied chemistry*, vol. 5, no. 1-2, pp. 37–52, 1962.
- [51] G. Chinga-Carrasco, "Cellulose fibres, nanofibrils and microfibrils: the morphological sequence of mfc components from a plant physiology and fibre technology point of view," *Nanoscale research letters*, vol. 6, no. 1, p. 417, 2011.
- [52] B.-J. De Gans, P. C. Duineveld, and U. S. Schubert, "Inkjet printing of polymers: state of the art and future developments," *Advanced materials*, vol. 16, no. 3, pp. 203–213, 2004.
- [53] P. M. Grubb, H. Subbaraman, S. Park, D. Akinwande, and R. T. Chen, "Inkjet printing of high performance transistors with micron order chemically set gaps," *Scientific reports*, vol. 7, no. 1, p. 1202, 2017.
- [54] F. Dimatix, "Materials printer & cartridges dmp-2831 & dmc-11601/11610," *Fujifilm Dimatrix, Santa Clara, USA*, 2008.
- [55] Z. Cui, *Printed electronics: materials, technologies and applications*. John Wiley & Sons, 2016.
- [56] D. K. Owens and R. Wendt, "Estimation of the surface free energy of polymers," *Journal of applied polymer science*, vol. 13, no. 8, pp. 1741–1747, 1969.
- [57] J. D. Berry, M. J. Neeson, R. R. Dagastine, D. Y. Chan, and R. F. Tabor, "Measurement of surface and interfacial tension using pendant drop tensiometry," *Journal of colloid and interface science*, vol. 454, pp. 226–237, 2015.
- [58] A. Merrington and E. Richardson, "The break-up of liquid jets," *Proceedings of the Physical Society*, vol. 59, no. 1, p. 1, 1947.
- [59] A. Lee, K. Sudau, K. H. Ahn, S. J. Lee, and N. Willenbacher, "Optimization of experimental parameters to suppress nozzle clogging in inkjet printing," *Industrial & Engineering Chemistry Research*, vol. 51, no. 40, pp. 13 195–13 204, 2012.

- [60] V. Ramachandran and H. S. Fogler, "Plugging by hydrodynamic bridging during flow of stable colloidal particles within cylindrical pores," *Journal of Fluid Mechanics*, vol. 385, pp. 129–156, 1999.
- [61] R. A. Street, W. Wong, S. Ready, M. Chabinyk, A. Arias, S. Limb, A. Salleo, and R. Lujan, "Jet printing flexible displays," *Materials Today*, vol. 9, no. 4, pp. 32–37, 2006.
- [62] H. Hillborg, J. Ankner, U. W. Gedde, G. Smith, H. Yasuda, and K. Wikström, "Crosslinked polydimethylsiloxane exposed to oxygen plasma studied by neutron reflectometry and other surface specific techniques," *Polymer*, vol. 41, no. 18, pp. 6851–6863, 2000.
- [63] M. Marzocchi, I. Gualandi, M. Calienni, I. Zironi, E. Scavetta, G. Castellani, and B. Fraboni, "Physical and electrochemical properties of pedot: Pss as a tool for controlling cell growth," *ACS applied materials & interfaces*, vol. 7, no. 32, pp. 17 993–18 003, 2015.
- [64] U. Kraft, F. Molina-Lopez, C. Zhu, Y. Wang, Z. Bao, and B. Murmann, "Inkjet-printed, intrinsically stretchable conductors and interconnects," in *Organic Field-Effect Transistors XVI*, vol. 10365. International Society for Optics and Photonics, 2017, p. 103650A.
- [65] H. L. Clever and C. Snead, "Thermodynamics of liquid surfaces: The surface tension of dimethyl sulfoxide and some dimethyl sulfoxide—acetone mixtures," *The Journal of Physical Chemistry*, vol. 67, no. 4, pp. 918–920, 1963.
- [66] M. Kuş and S. Okur, "Electrical characterization of pedot: Pss beyond humidity saturation," *Sensors and Actuators B: Chemical*, vol. 143, no. 1, pp. 177–181, 2009.
- [67] E. S. Muckley, C. B. Jacobs, K. Vidal, J. P. Mahalik, R. Kumar, B. G. Sumpter, and I. N. Ivanov, "New insights on electro-optical response of poly (3, 4-ethylenedioxythiophene): poly (styrenesulfonate) film to humidity," *ACS applied materials & interfaces*, vol. 9, no. 18, pp. 15 880–15 886, 2017.
- [68] M. Döbbelin, R. Marcilla, C. Tollan, J. A. Pomposo, J.-R. Sarasua, and D. Mecerreyes, "A new approach to hydrophobic and water-resistant poly (3, 4-ethylenedioxythiophene): poly (styrenesulfonate) films using ionic liquids," *Journal of Materials Chemistry*, vol. 18, no. 44, pp. 5354–5358, 2008.
- [69] L. Biessmann, L. P. Kreuzer, T. Widmann, N. Hohn, J.-F. Moulin, and P. Muller-Buschbaum, "Monitoring the swelling behavior of pedot: Pss electrodes under high humidity conditions," *ACS applied materials & interfaces*, vol. 10, no. 11, pp. 9865–9872, 2018.
- [70] J. Huang, P. F. Miller, J. S. Wilson, A. J. de Mello, J. C. de Mello, and D. D. Bradley, "Investigation of the effects of doping and post-deposition treatments on the conductivity, morphology, and work function of poly (3, 4-ethylenedioxythiophene)/poly (styrene sulfonate) films," *Advanced Functional Materials*, vol. 15, no. 2, pp. 290–296, 2005.
- [71] B. Andres, C. Dahlström, N. Blomquist, M. Norgren, and H. Olin, "Cellulose binders for electric double-layer capacitor electrodes: The influence of cellulose quality on electrical properties," *Materials & Design*, vol. 141, pp. 342–349, 2018.
- [72] L. A. Pettersson, S. Ghosh, and O. Inganäs, "Optical anisotropy in thin films of poly (3, 4-ethylenedioxythiophene)–poly (4-styrenesulfonate)," *Organic Electronics*, vol. 3, no. 3-4, pp. 143–148, 2002.